UNIVERSITY OF OKLAHOMA
GRADUATE COLLEGE

IMPACT OF ASSIMILATING GROUND-BASED AND AIRBORNE RADAR OBSERVATIONS FOR THE ANALYSIS AND PREDICTION OF THE EYEWALL REPLACEMENT CYCLE OF HURRICANE MATTHEW (2016) USING HWRF HYBRID 3DENVAR SYSTEM

A THESIS
SUBMITTED TO THE GRADUATE FACULTY
in partial fulfillment of the requirements for the
Degree of
MASTER OF SCIENCE IN METEOROLOGY

By

TYLER GREEN
Norman, Oklahoma
2021

IMPACT OF ASSIMILATING GROUND-BASED AND AIRBORNE RADAR OBSERVATIONS FOR THE ANALYSIS AND PREDICTION OF THE EYEWALL REPLACEMENT CYCLE OF HURRICANE MATTHEW (2016) USING HWR HYBRID 3DENVAR SYSTEM

A THESIS APPROVED FOR THE
SCHOOL OF METEOROLOGY

BY THE COMMITTEE CONSITING OF

Dr. Xuguang Wang, Chair

Dr. Benjamin A. Schenkel

Dr. Michael I. Biggerstaff

Acknowledgments

First, I want to thank Dr. Xuguang Wang for giving me the opportunity to work on a project related to tropical cyclones, which is near and dear to my heart being born and raised on the east coast of Florida. I want to extend a very special thank you to Xu Lu for his patience and dedication to helping me learn the HWRF modeling system and fielding a multitude of questions from me on a daily basis. Xu gave up so much of his time in order to help me and was always happy to do so, and for that I will always be grateful. I also want to extend a special thank you to Ben Schenkel for his time, guidance and advice throughout the last year of my studies and for giving me some of the pushes I needed to get across the finish line. Lastly, I want to thank my friends and family who supported me during my time in Norman, especially my Fiancée Michelle, who has seen both the good and the bad times but has supported me every step of the way.

Table of Contents

List of Tables

List of Figures

Abstract

Eyewall replacement cycles (ERC) are common dynamical processes in mature tropical cyclones (TCs) that can result in quick changes to the storm's intensity and wind field size. As the resolution of TC models increases, accurate initializations of concentric eyewall (CE) structure through advanced data assimilation (DA) are hypothesized to be important to capture the ERC and the associated rapid intensity change by numerical models. In this study, the analysis and prediction of Hurricane Matthew's (2016) ERC is examined using HWRF and a Hybrid 3D Ensemble-Variational DA scheme. Four experiments performing hourly DA cycling from 1500 UTC October 6 to 1500 UTC October 7 are performed, assimilating different sets of inner-core doppler radar radial velocity observations, including Tail-Doppler Radar (TDR), coastal Ground-Based Radar (GBR), and their combination. The primary scientific objective of this study is to assess the impacts of assimilating GBR and TDR radial velocity observations individually, and in combination, on the analysis and forecast of Matthew during the weakening and reintensification phase of its ERC.

Results show that the earlier availability and continuous coverage of GBR observations is needed to make quick corrections to initialize CE structure, even with limited lower-level coverage of the storm. The subsequent forecasts from the experiments assimilating GBR observations demonstrated the capability to make *realistic* and *consistent* forecasts of the structural and intensity changes associated with the ERC. The TDR experiment revealed that as a result of the later start and shorter duration of inner core doppler radar observation availability, the analyses' structure throughout the cycling period was not as realistic compared to the expected structural changes of the ERC, as were the GBR and GBTDR experiments. This is hypothesized to be a result of the varying horizontal coverage of TDR observations within the DA time window from analysis time to analysis time during high frequency DA cycling. As a result of this, the TDR forecasts did not show the ability to consistently capture the correct structural and intensity changes during the ERC. With no assimilation of ICDR observations, the Control experiment demonstrated no ability to make correct analyses and forecasts of Matthew's CE structure and ERC. The importance of correctly initialized structure was highlighted by showing that the evolution of the primary and secondary eyewall structure is consistent with balanced and unbalanced dynamics in an axisymmetric framework. Proper initialization of the secondary eyewall governs the evolution of

the ERC by restricting high angular momentum air from reaching the primary eyewall, acting to contract and intensify the secondary eyewall and spin down the primary eyewall.

1. Introduction

Improvements in intensity prediction for tropical cyclones (TC) has notably lagged behind the advances made in TC track predictions over the last few decades (Landsea & Cangialosi, 2018). However, over the last decade, and in large part due to advancements made in the Hurricane Forecast Improvement Program (Gall et al., 2013), the skill of intensity predictions from dynamical models has started to increase. As a result of this, they have become competitive with statistical-dynamical models which have consistently been the most skillful (Cangialosi et al., 2020). Dynamical models continue to struggle with the prediction of large intensity fluctuations caused by processes such as rapid intensification (RI) and eyewall replacement cycles (ERCs). Since large intensity changes are thought to originate from TC inner core dynamics (Gall et al., 2013), improvements to the horizontal grid spacing, model parameterizations, and analyzed storm structure due to superior data assimilation (DA) techniques should provide more accurate forecasts for these events. For example, the Hurricane Weather Research and Forecasting (HWRF) model has had a positive trend in its probability of detection rate of RI events since its inception in 2007 (Cangialosi et al., 2020). This is likely due to the gradual decrease in its grid spacing of the innermost nest (currently at 1.5 km) allowing for improved resolution of inner core dynamics. In addition, superior DA techniques with the assimilation of inner core Tail-Doppler Radar (TDR) observations (Lu et al., 2017a,b) help to improve analyzed storm structure. However, a limitation to better predictions of these events continues to be the lack of understanding of the dynamics underlying rapid intensity changes in TCs.

The ERC is a common process in mature TCs which acts to modulate their intensity and wind field size. TCs that undergo this process are characterized by concentric eyewalls (Houze et al., 2007; Sitkowski et al., 2011; Willoughby et al., 1982). With a large set of aircraft reconnaissance data, Sitkowski et al. (2011) demonstrated that most ERCs could be broken into three distinct phases. The first, labeled “intensification”, occurs when a secondary wind maximum develops radially outward of the primary wind maxima, contracting inward while it intensifies. This phase is completed when the primary wind maximum reaches its peak intensity. The second phase, or “weakening” phase, is characterized by the secondary wind maxima continuing to contract and intensify, ending when the intensity of the secondary wind maxima reaches that of the primary wind maximum. Lastly, the third phase, or “reintensification” phase, is marked by the further intensification of the secondary wind maximum, while the primary wind maximum begins to decay. When the primary wind maximum is no longer detected, the ERC is considered complete. The TC is left with the former secondary wind maxima as the new primary wind maxima which usually resides at greater radius than the original primary eyewall. This new primary wind maxima can then begin to contract and intensify. In most cases, ERCs lead to the broadening of the TC vortex (Maclay et al., 2008; Sitkowski et al., 2011) which can have forecasting implications depending on the TC's proximity to land (Irish et al., 2008). This was the case for two notable hurricanes, Katrina (2005) and Ike (2008). Both storms weakened before landfall as a result of an ERC but saw an expansion of their wind fields which affected the spatial extent of storm surge impacts (*Creating a New Suite of Statistical Models that Predict the Onset of an Eyewall Replacement Cycle*, n.d.).

Currently, the only objective tool available to forecasters for predicting the onset and intensity/structural changes associated with ERCs are statistical models (Kossin & Sitkowski, 2009, 2012). Successful modeling of ERC events is therefore important for the advancement of TC intensity prediction. In addition to successful prediction of ERC events with dynamical modeling, the development of advanced DA techniques is expected to provide more realistic analyzed TC structure to help identify when a TC is likely to undergo intensity changes associated with ERCs. Most of the modeling studies of ERC's focus on the mechanisms responsible for a certain phase or phases of the ERC (Didlake et al., 2017), with the most frequent one being secondary eyewall formation (SEF) given its importance for the subsequent intensity changes. The mechanisms responsible for SEF are not fully agreed upon and are less understood than the other phases of the ERC (Fischer et al., 2020). Modeling studies of ERCs have consisted of both idealized (Kepert, 2013; Rozoff et al., 2008; Terwey & Montgomery, 2008; Wang, 2008a,b; Zhou & Wang, 2009,2011) and real cases (Abarca & Corbosiero, 2011; Houze et al., 2007; Zhang et al., 2005). Of the modeling studies for real cases, there has been a focus on the ability of the model to capture key features of the ERC, but not on the accuracy of ERC predictions in terms the timing of phase changes and the overall morphology of the structure in comparison with observations. For example, Abarca & Corbosiero (2011) and Houze et al. (2007) demonstrated that key features of the ERC conceptual model such as the establishment of a secondary eyewall, contraction of the secondary eyewall, and decay of the primary eyewall could be captured in their numerical simulations of Hurricanes Katrina and Rita, respectively. This proved that convection allowing models are able to capture key processes associated with the ERC. These early studies, however, did not examine how realistic the forecasts were compared to observations during the ERC. One of the goals of this study is to investigate the ability of HWRF, with the advanced assimilation of inner core doppler radar observations, to predict an ERC event and make realistic analyses of concentric eyewall (CE) structure for a real case of Hurricane Matthew (2016).

In order to obtain the accurate prediction of ERC events, more accurate analyses of TC kinematic and thermodynamic structures are expected to be needed to initialize the numerical model through the advancement of data assimilation. Over the last decade, the implementation of ensemble-based DA for TC prediction (Aksoy et al., 2012, 2013; Dong & Xue, 2013; Li et al., 2012; Lu, et al., 2017a,b; Torn, 2010; Weng & Zhang, 2012; Zhang et al., 2009) along with the assimilation of high-resolution TC inner core observations has shown promises for TC prediction. More skillful intensity predictions as well as more realistic analyzed and predicted storm structure are demonstrated by assimilating the aircraft-born TDR observations for both case (Aksoy et al., 2012; Lu, Wang, Tong & Tallapragada, 2017; Weng & Zhang, 2012) and systematic studies (Aksoy et al., 2013; Zhang et al., 2011; Lu et al., 2017). Another source of high spatial and temporal resolution inner core observations is from the coastal ground-based radar surveillance stations (hereafter GBR for "ground-based radar") that can sample TCs near and during landfall. Numerous studies have shown improvements to the analyzed TC structure and intensity forecasts after the assimilation the GBR observations (Dong & Xue, 2013; Li et al., 2012; Wang et al., 2014, 2015; Zhao & Xue, 2009; Zhang et al., 2009; Zhu et al., 2016).

Most of the studies assimilating TDR or GBR observations have focused on the general improvements of the track and intensity forecasts and how improvements to analyzed structure contribute to these. Different from these early studies, this study places an emphasis on exploring the impact of assimilating these observations on the prediction specifically associated with the ERC process. During the ERC of Hurricane Matthew, it was sampled by both GRB and TDR with differing temporal availabilities. Another goal of the study is to investigate the relative impact of assimilating the TDR and GBR observations on the prediction of the ERC process of Matthew. To the author's best knowledge, studies comparing these two sources of data for hurricane prediction are limited. HWRF has assimilated TDR observations operationally since 2013 (Sippel, 2019) while GBR observations began operational use in 2020 (J. Sippel, personal communication, July 9, 2021). Each set of observations offers their own benefits and drawbacks which are listed in

Observation Type	Benefits	Drawbacks
TDR	o Availability over open waters and long distances away from land o More frequently available on case-by-case basis, especially for strong TCs o More uniform 3D spatial coverage of TC during flight penetration legs (Aksoy et al., 2012)	o Lack of availability as TCs approach landfall o Limited to Atlantic and East Pacific Basins o Asymmetric 3D spatial coverage of TC during flight downwind legs (Aksoy et al., 2012)
GBR	o Continuous availability when TC is in close proximity to land o GBR networks available in other basins such and Indian Ocean and West Pacific, and in remote locations such as Puerto Rico	o Only available for storms that track close to land o Less uniform 3D spatial coverage of TC due to fixed nature of radar stations

Table 1.1: Benefits and drawbacks of the two different inner core doppler radar observations used

Table 1.1. The relative impact of assimilating the GBR and TDR observations for TC prediction specifically associated with the ERC process is left unanswered. This study makes the first attempt to address this question.

As mentioned earlier, SEF tends to be the most studied phase of the ERC. When ICDR observations became available for Hurricane Matthew, a secondary eyewall was already clearly established as evidenced by its reflectivity structure from the Miami, FL WSR-88D radar and the NOAA WP-3D aircraft's lower fuselage radar. Therefore, the mechanisms for and prediction of SEF is not the focus of the study. However, the ability of the DA cycling to establish CE structure resembling observations, and the impact of such an establishment on the subsequent forecasts are still important steps toward the improvement of TC intensity forecasts associated with ERCs. The scope of this study is therefore specifically confined to DA cycling throughout the ending of the weakening phase and entirety of the reintensification phase up to the completion of the ERC. An in-depth description of Matthew’s ERC and phases is given in Section 2.

In this study, the analysis and prediction of Hurricane Matthew’s ERC are examined using HWRF and an hourly, continuously cycled hybrid 3D ensemble-variational (3DEnVar) DA scheme with the assimilation of GBR and TDR radial velocity observations as the storm paralleled Florida’s east coast on October 6-7, 2016. The primary scientific objectives of this study are to: Assess the impacts of assimilating GBR and TDR radial velocity observations individually, as well as in combination, on the analysis and forecast of Hurricane Matthew’s concentric eyewall structure and evolution throughout the weakening and reintensification phases of the ERC.

The remainder of this study is outlined as follows. Section 2 discusses Hurricane Matthew and its ERC evolution in depth, as well as the experimental setup, DA specifics, and detailed information on the GBR and TDR observations. In Section 3, the results of experiments performing continuous cycling with different ICDR observations are discussed to address the scientific objectives of this study. Section 4 concludes the study with a summary of the results. In addition, a discussion of a potential caveat of the simultaneous assimilation of the two different ICDR observation types is provided, along with suggestions for their more effective use in the future for the analysis and prediction of TCs with intricate kinematic structures.

2. Data and Methods

2.1 Hurricane Matthew

Hurricane Matthew was the 14th named storm of the 2016 Atlantic Hurricane season, setting a record for achieving category 5 intensity at the lowest latitude in the Atlantic Basin (Stewart, 2017). At the time Matthew became the deadliest Atlantic hurricane since 2005, responsible for 585 deaths, with a large majority of these occurring in Haiti (Stewart, 2017). On October 6-7, 2016, Matthew paralleled Florida's East coast while undergoing an ERC that was sampled by coastal WSR88D radars in Miami, Melbourne, and Jacksonville. Matthew's composite reflectivity evolution is shown in Figure 2.1, where a transition from a concentric to single eyewall structure is evident. Figure 2.1B displays a classic CE structure in composite reflectivity at 1808 UTC October 6, with both eyewalls being symmetric and the primary eyewall centered in the middle of the second. Through the rest of Matthew's ERC evolution, the primary eyewall exhibits an azimuthal wavenumber 1 pattern with convection occurring in the downshear left quadrant (Corbosiero & Molinari, 2003) while slowly decaying and becoming nonexistent by 1500 UTC October 7. The secondary eyewall oscillates between an axisymmetric (Figure 2.1B,I) and asymmetric (Figure 2.1D,F) structure throughout the ERC evolution. The secondary eyewall eventually replaces the former primary eyewall at a wider radius than the original (Figure 2.1I).

To provide a more quantitative description of Matthew's structural changes associated with the ERC, the methodology of Sitkowski et al. (2011) is used with slight modifications[1] to track the evolution of the radius and intensity of the primary and secondary eyewalls from flight-level[2] reconnaissance (FL RECON) wind observations. Figure 2.2A and 2.2B show the radius and intensity, respectfully, of each eyewall as a function of time with cubic polynomials fit to the data using least squares to show trends of each parameter. These cubic fits (CFs) will be used throughout the rest of the study as proxies for the location of the primary and secondary eyewalls and to identify the correct trends in intensity forecasts. They are also used to identify when the ERC changes from the weakening to reintensification phase. This is marked by the time the CF of the primary and secondary eyewalls' intensity intersect, indicating the secondary eyewall has

---

[1] Flight level winds are not pressure-adjusted to a reference level.

[2] Flight level is approximately 700 hPa or 3 km above ground level. The flight-level height varies depending on the intensity of the TC.

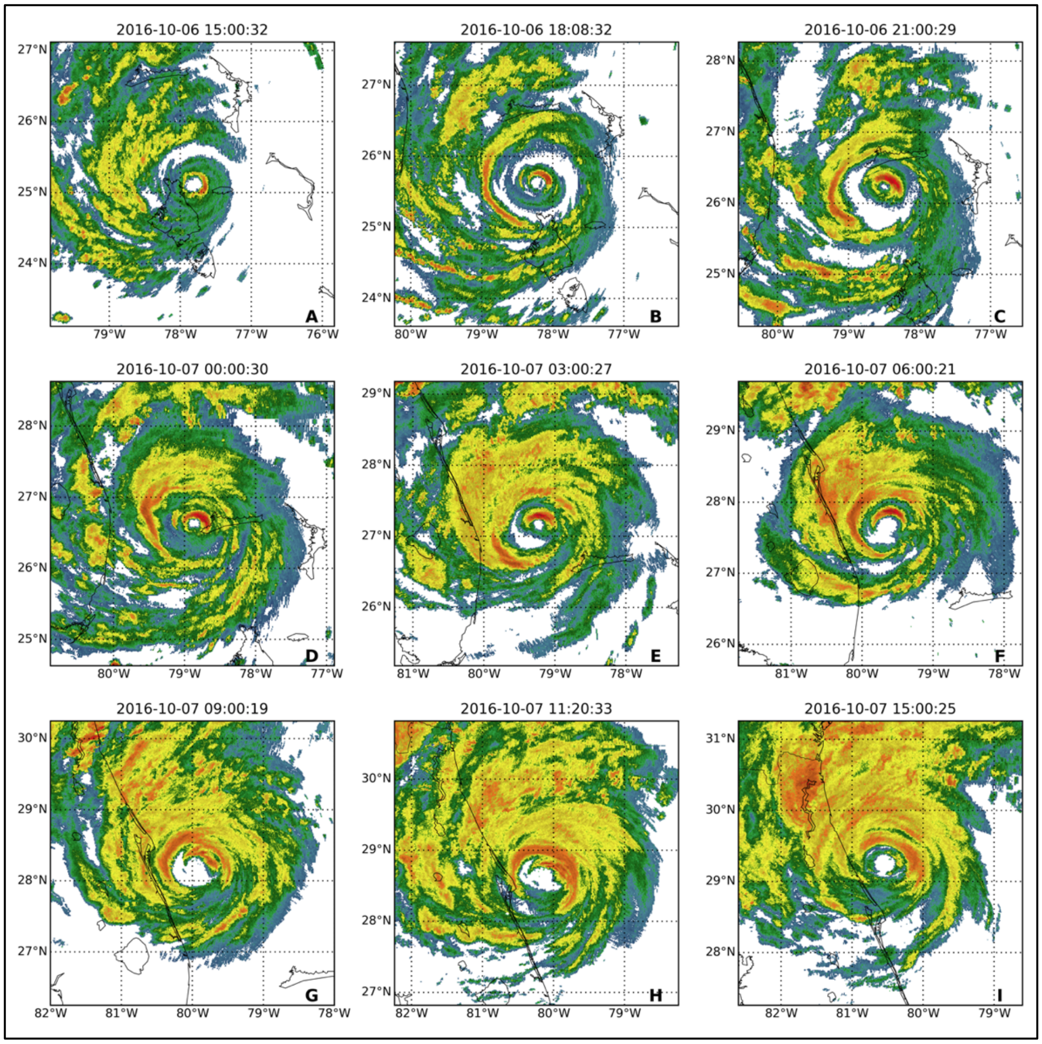

Figure 2.1: MRMS composite reflectivity of Hurricane Matthew approximately every three hours from 1500 UTC October 6 to 1500 UTC October 7. The evolution of the composite reflectivity shows a transition from concentric to single eyewall structure.

surpassed the primary eyewall in intensity. The time of this phase change is not highly sensitive to perturbations in the wind intensity data shown in Figure 2.2B. Given the use of the CFs in this study, the variability of the wind intensity and radius data in Figure 2.2 must be acknowledged. Variability in the radius data is smaller compared to the wind intensity data and is likely due to structural asymmetries in the eyewalls (elliptical vs annular). The variability of the wind intensity data arises from the intensity differences from different quadrants of the TC. Errors associated with the methodology used to calculate the wind and radii parameters are inherent, however, they do not account for the total variability in the penetration legs through Matthew's inner core.

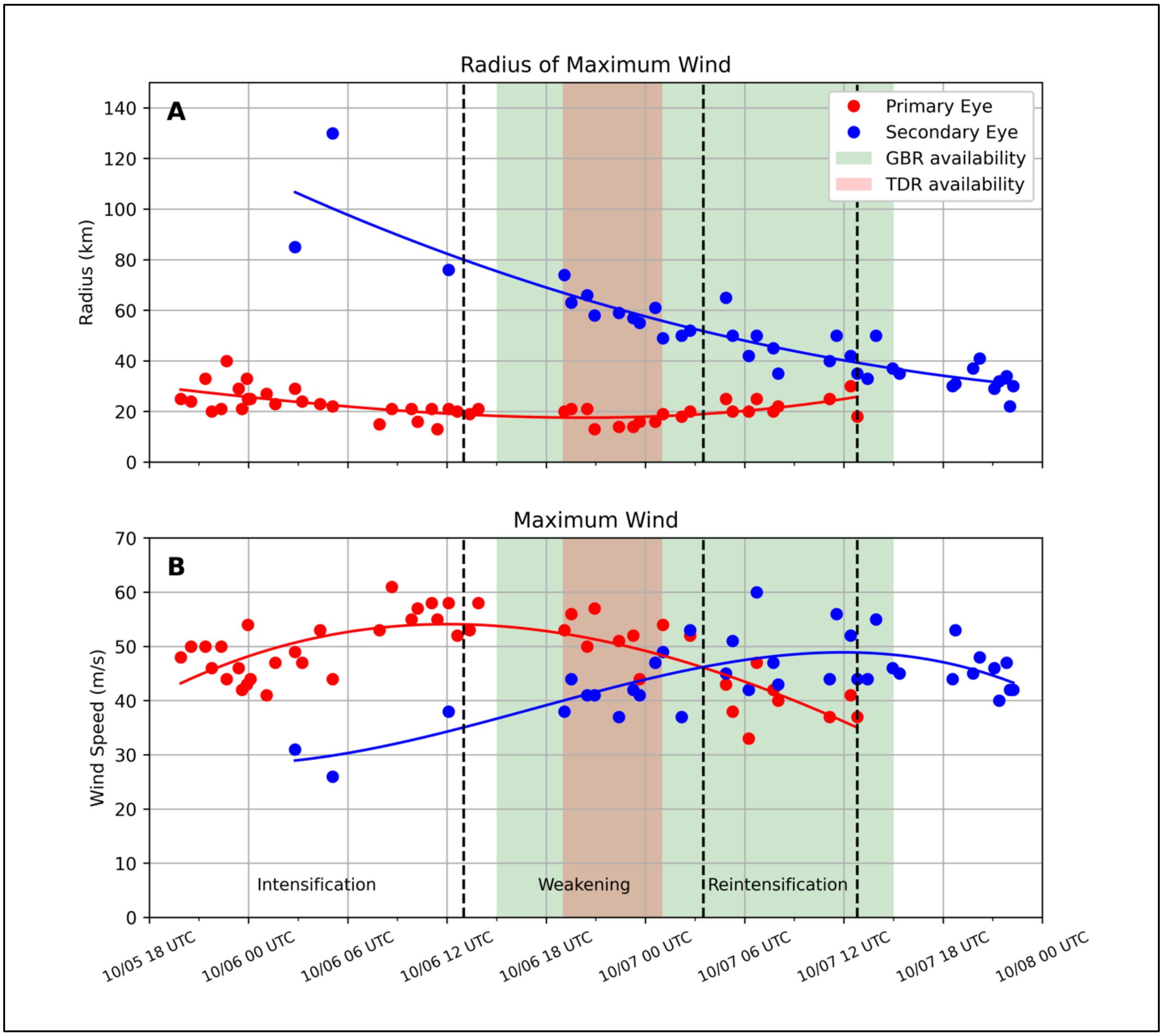

Figure 2.2: Evolution of radius (A) and intensity (B) of Hurricane Matthew's primary and secondary wind maxima from FL RECON data calculated using the methodology of Sitkowski et al. (2011). The different phases of the ERC as determined by the aforementioned methodology are labeled and bounded by black vertically dashed lines. Cubic polynomials are fit to the radius and intensity for both wind maxima using least squares to show trends in their evolution. Color shadings in the background of both panels represent the temporal availability of ICDR observations, with the extent of the GBR availability representing the entire hourly cycling duration.

The time period focused on in this study is from 1500 UTC October 6 to 1500 UTC October 7 (corresponding to the green shaded area representing the GBR availability), however, the evolution of the ERC is also discussed leading up to this period for background. Evidence of a secondary wind maximum is first seen around 0300 UTC October 6 at a radius of 80-120 km

(Figure 2.2A). Up to just before the start of GBR availability, around 1300 UTC October 6, Matthew is in the intensification phase, with the primary eyewall radius slowly contracting from about 30km to 20km while intensifying from about 45 to 55 m/s. The secondary wind maximum was apparent only 3 times during this phase, but from the CF, the secondary wind maximum appears to be contracting and intensifying. The start of the weakening phases happens immediately after the primary eyewall reaches its maximum intensity, around 1300 UTC October 6, and is marked by the first black vertically dashed line in Figure 2.2. Matthew's secondary eyewall continues to contract and intensify in this phase while the primary eyewall weakens. The two eyewalls equal each other in intensity around 0300 UTC October 7, signifying the end of the weakening phase and start of the reintensification phase. Matthew's secondary eyewall continues to contract and strengthen further during the reintensification phase, with the primary eyewall eventually being last detected around 1300 UTC October 7, marking the end of the ERC. GBR observations are available during both the weakening and reintensification phases of the ERC, while the TDR availability is limited to the period from 1900 UTC October 6 to 0100 UTC October 7. More details about the GBR and TDR observations and their spatial and temporal distributions are given in Section 2.3.

2.2 Model/Data Assimilation Description and System Configuration

The 2018 version of the HWRF model (Biswas et al., 2018) is used in this study. A 40-member ensemble is used, with each member consisting of a parent domain (D01) with resolution of 0.099˚ (13.5 km) and a 2-way moveable nested domain (D02) with resolution of 0.033˚ (4.5 km). One control member is used, with similar grid configuration to the ensembles, but with one more 2-way moveable domain (D03) nested inside D02 with resolution of 0.011˚ (1.5 km). Running the ensembles and control with two different grid spacings in this manner is referred to as dual resolution. HWRF uses the Non-Hydrostatic Mesoscale Model (NMM) dynamical core on a rotated E-grid. A hybrid vertical coordinate is used with 75 model levels and a model top of 10 hPa (Biswas et al., 2018). Its physical parameterizations are specific for use in tropical cyclone applications, with the ones used in this study are as follows: Ferrier microphysical scheme, Rapid Radiative Transfer Model for Global Circulation Models radiation scheme, Noah Land-Surface Model, NCEP Global Forecast System boundary-layer scheme and Simplified Arakawa-Schubert deep and shallow convection scheme (Biswas et al., 2018). All boundary conditions for both the control and ensembles' D01 are obtained from the GFS. In this study, the ocean coupling component is turned off, and the vortex initialization (VI) procedure differs from normal operational use. The VI differences in this study are discussed in the next paragraph. For the 3DEnVar DA system, localizations of 60km and 550 hPa (Li et al., 2012) are used for horizontal and vertical localizations respectively. In this study, the full weight is assigned to the flow dependent background error covariance (BEC), meaning it is obtained exclusively form the 40-member ensemble. The Ensemble Kalman Square Root Filter (EnSRF) uses a 500 km and 400 hPa (Li et al., 2012) horizontal and vertical localization respectfully, with an adaptive covariance inflation factor of 0.9 used for mitigation of filter divergence.

The experiments in this study are run using the continuously cycled, dual resolution hybrid 3DEnVar system developed by Lu et al. (2017b). The basic steps for running the 6-hour cycling (operationally used) are explained first. Following that, the specific modifications and changes to the 6-hour cycling for the experiments in this study are detailed. In addition to this, and before continuing, HWRF's VI procedure is briefly discussed. The VI procedure consists of two components that are usually run before DA is performed. The first is vortex relocation (VR) which corrects the storm's location, usually based on a Tropical Cyclone Vitals (TCVital) message valid at the analysis time. The second is vortex modification (VM) which corrects the structure and intensity of the storm based off of parameters such as minimum sea level pressure, maximum wind, and radius of multiple different wind intensities. These parameters are also taken from the TCVital message. For a more in-depth description of the VI procedure, the reader is referred to Biswas et al. (2018). The 6-hour cycling system is now detailed.

For the first cycle of the storm in the 6-hour 3DEnVar DA system, the ensembles and control are initialized from the operational GFS ensemble and control analyses. A 6-hour cold start forecast is then launched for the ensemble members, and a 9-hour forecast for the control member using the directed moving next strategy (Lu et al., 2017b). VI is then performed on the 6-hour ensemble forecasts (VR only) and on the 3,6, & 9 hour control forecasts (VR & VM). DA is then performed simultaneously on the control and ensemble members. For the 40 ensembles, only D02 is updated by EnSRF. For control domains D02 and D03, the backgrounds are updated by the hybrid 3DEnVar technique through the minimization of a 3D cost function with the BEC obtained exclusively from the ensembles, as mentioned earlier. For the control, the First Guess at

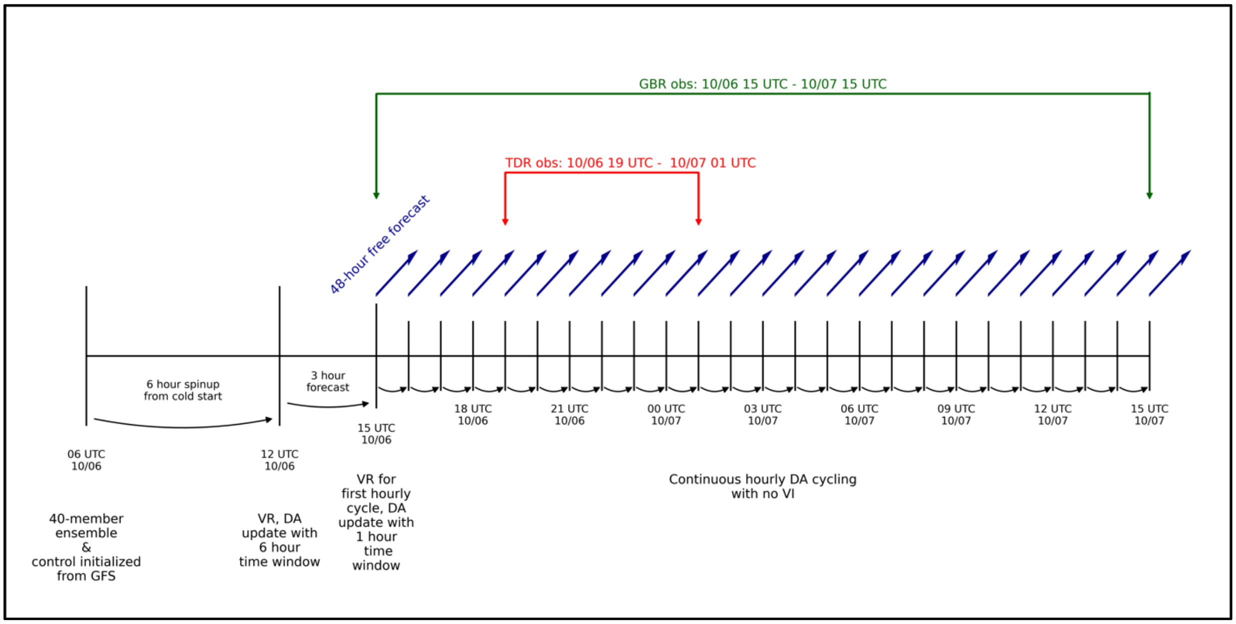

Figure 2.3: Flowchart showing configuration of the DA cycling performed for all experiments.

Appropriate Time (FGAT) (Fisher & Anderson, 2001) method is used due to the large time window, and is the reason the control backgrounds are also outupt at 3 and 9 hour forecast times. Following the DA updates, the ensemble members are recentered around the D02 control analysis, meaning the ensemble mean from EnSRF is replaced with the control analysis. Lastly, the parent domains (D01) for the ensembles and control are replaced by the GFS analyses at that time due to better initialization of the large scale environment by the global model. To start the next cycle, the forecasts for the ensmebles and control are launched and the steps above are repeated. In addition, free forecasts, usually of 126 hours, are launched from the control analysis, providing a deterministic forecast for the cycle.

The main differencse between the cycling system used in this study and the one detailed above is the cycling frequency and the use of VI. Here, the cycling is more frequent, 1 hour instead of 6 hours, and uses a 1 hour time window (+/- 30 minutes from the analysis time). The FGAT method is not used given temporal proximity of observations in the time window to the analysis time, making the assumption that all observations are valid at the analysis time. The second main difference is the use of VI and when it is used. To help visualize the configuration of cyling for all experiments in this study, a flowchart is shown in Figure 2.3. A cold start is initialized by the GFS for the ensembles and control on October 6th at 0600 UTC. A 6 hour forecast (9 hours for control) is run to October 6th at 1200 UTC, followed by VR and DA updates with a 6 hour time window using FGAT with only "conventional observations" (no ICDR observations). Specific observations assimilated will be discussed in more detail in Section 2.3. After this, a 3 hour forecast for the ensembles and control is run to 1500 UTC October 6th which marks the start of hourly cycling and availability of GBR observations. By this time, the covraince strucutre in the 40 member ensmeble has had enough time to evolve.

Before the hourly cycling is done, VR is performed at 1500 UTC October 6 with the position taken from a linear interpolation of the TCvital messages from 1200 UTC and 1800 UTC October 6. This is the last time VR is performed. For the next 24 hours up to 1500 UTC on October 7th, hourly DA cycles are performed (Figure 2.3), assimilating respective observations for both inner core and conventional based on the experiment. After DA is performed each hour, a 48-hour free forecast is launched from the analysis time with hourly output. The length of the free forecast is noteably shorter than the 126 hour free forecast that is normaly performed in TC modeling studies. The focus on short term forecasts of Matthew's ERC negates the need for longer forecasts in this case. Details on the four different cyling experiments along with the ICDR observations are discussed next.

2.3 Description of Experiments and ICDR Observations

To address the scientific objectives for this study, four different experiments will be performed following the flow chart in Figure 2.3. Each experiment is identical up to the 1500 UTC October 6 analysis time, after which the experiments perform hourly cycling with different sets of observations available to them. Before detailing the observations assimilated in the four experiments, we define the phrase "conventional observations" as the combinations of all available observations from the following files obtained from the operational datastream: prepbfur, satwndbufr, tcvital, and satellite radiances. No observations from dropsondes or FL RECON are assimilated by any experiment in this study.

The first experiment, "Control", will only assimilate the conventional observation set, providing a baseline for comparing experiments with ICDR observations to. The second experiment is called "GBR", for ground-based radar, which assimilates the conventional observations along with GBR radial velocity observations. The third experiment is called "TDR" for Tail-Doppler radar and assimilates the conventional observations along with TDR radial velocity observations when they are available. No GBR observations are assimilated in the TDR experiment. The last experiment is called "GBTDR" which assimilates the conventional observations, GBR radial velocity observations, and TDR radial velocity observations. The four experiments will allow assessments of the relative impacts of assimilating different ICDR observation types together and separately, in addition to not assimilating any ICDR observations at all, on the accuracy of the analyses and forecasts for Matthew.

Differences in temporal availability and 3D coverage of GBR and TDR radial velocity observations affect the evolution of storm structure during hourly cycling, with each of the two having their own benefits and drawbacks as discussed in Section 1. The differences in availability of the GBR and TDR observations are stark, as the GBR observations are available and provide coverage of Matthew's inner core for the entire 24-hour cycling period. The TDR, in comparison, only covers about a 7-hour period from 1900 UTC October 6 to 0100 UTC October 7, which is a typical duration of any TDR mission into TCs. In addition to this, distinct differences in the 3D observation distribution between GBR and TDR exist and are shown in Figure 2.4. Starting with GBR, the changes in horizontal and vertical observation distributions are tied to the motion of Matthew and its storm track relative to radars along Florida's east coast. At the early cycling times, GBR observations peak in vertical density (vertical observation densities only consider observations within 100 km of the storm center) around 7.5 km above ground level (AGL) (Figure 2.4B) and peak in horizontal density roughly 225 km from the storm center (Figure 2.4A). This is due to fixed nature of the GBR stations and Matthew's distance away from the nearest site at these times. As cycling continues, the number of observations within 100 km of the storm center increases while the peak vertical density starts to move to lower elevations as more GBR observations are available at all vertical levels (Figure 2.4B). The peak in vertical density of observations still exists at higher elevations (around 6 km AGL at 1500 UTC October 7) at the end of the hourly cycling.

The peak horizontal distribution of observations, in general, is shifted radially inward as the cycling continues, and as Matthew approaches closer to land (Figure 2.4A). The TDR has less uniform changes in horizontal and vertical observation distributions from analysis time to analysis time. The horizontal distributions of TDR observations for the 7 available cycles show large changes from hour to hour in the radius of peak density. The reason for this is the nature of the flight's butterfly pattern (see Fig 2 of Aksoy et al., (2012)). When the flight is in a penetration leg,

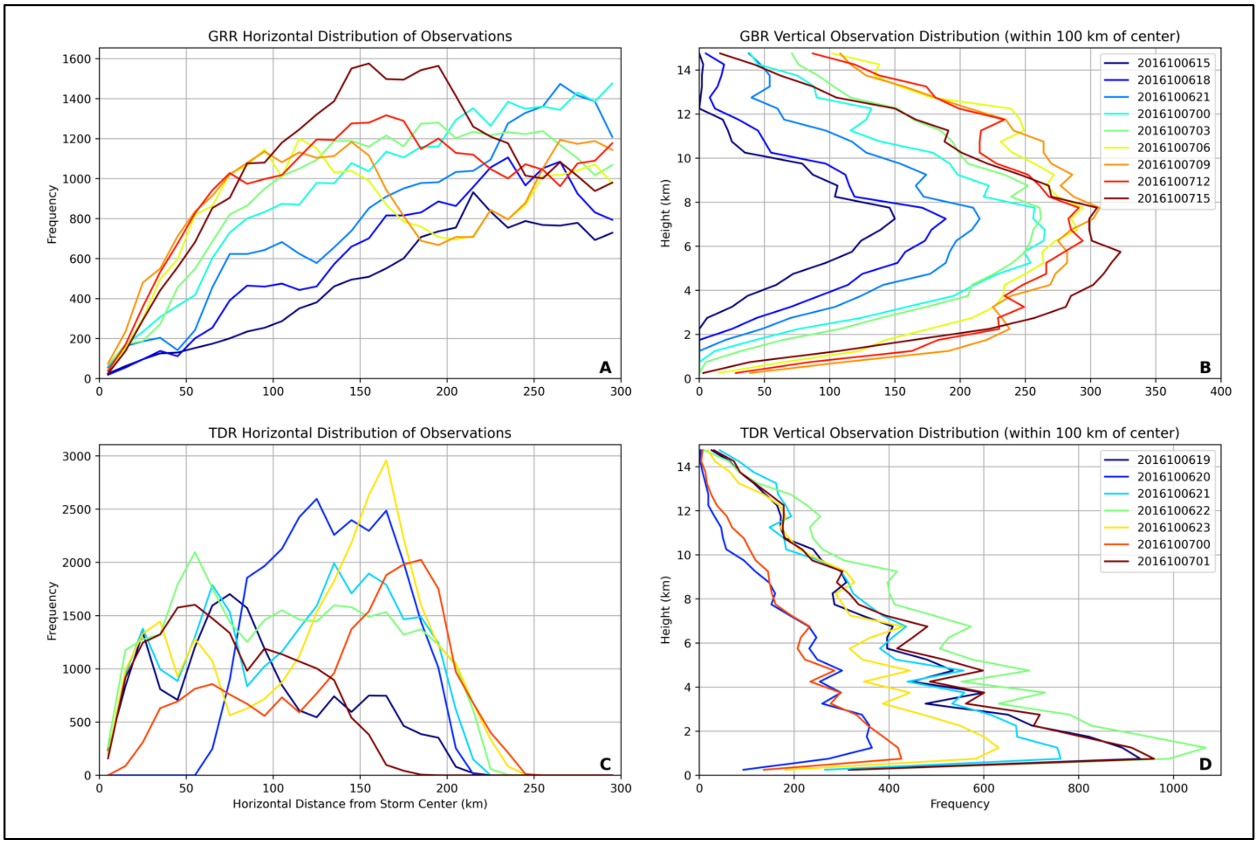

Figure 2.4: Horizontal (left column) and vertical (right column) distributions of GBR (top row) and TDR (bottom row) radial velocity observations for select analysis times (every 3 hours for GBR and every hour for TDR). For vertical distributions, only observations withing 100 km of the storm center are considered. Note that similar colored lines between the GBR and TDR distributions are not an indicator that they are from the same analysis time.

the horizontal distribution of TDR observations will peak near the storm center, for example at 1900 UTC October 6. Alternatively, when the flight is in a downwind leg, the horizontal distribution will peak farther out from the storm center, for example at 0000 UTC October 7. The vertical distribution of TDR observations does not change in shape during the analysis times, but differences in the amount of observation withing 100 km of the storm center are apparent (Figure 2.4D). The peak in vertical distribution of TDR observations occurs between 0-2 km AGL for each analysis time shown, with the number of observations within 100 km of the storm center being inversely correlated to the radius at which horizontal distribution peaks.

In summary, GBR observations have continuous temporal coverage throughout the cycling period. Their spatial distribution starts out poor, with max vertical and horizontal observation densities in the middle levels and larger radii, respectively. Their 3D spatial distribution slowly improves over the cycling time as Matthew comes closer in proximity to land, leading to more observations near the storm center horizontally, and better coverage of the lower levels. The TDR observations have less temporal availability but do offer better vertical coverage during flight penetration legs. When the aircraft is in a downwind leg during the DA window, the horizontal distribution of observations is poor. Overall, these discussed differences aid in the interpretation of results from the continuous cycling.

GBR observations are available from 5 different WSR-88D locations for each hourly cycle. For the first 12 hours of cycling (1500 UTC October 6 to 0200 UTC October 7) GBR observations are used from Key West, FL (KBYX), Miami, FL (KAMX), Melbourne, FL (KMLB), Tampa Bay, FL (KTBW), and Jacksonville, FL (KJAX). For the last 12 hours of cycling (0300 UTC October 6 to 1500 UTC October 7), Charleston, SC (KCLX) observations are assimilated and KBYX observations are dropped. To obtain the GBR observations, Level 2 radar data are postprocessed using Py-ART software (Helmus & Collis, 2016) to perform quality control and dealiasing with the "regional" method. Following this, an additional manual check is performed to ensure poorly dealiased scans are removed. TDR observations are obtained from the NCEP operational datastream, which have already been quality controlled and dealiased. Both GBR and TDR observations are assigned an observation error of 3 m/s used for DA.

3. Results

3.1 Analysis of Matthew's Concentric Eyewall Structure and Storm Evolution

The focus of this section is to assess how accurately Matthew's concentric eyewall structure and evolution during the weakening and reintensification phases can be analyzed using consecutive DA cycling from 1500 UTC October 6 to 1500 UTC October 7 with assimilation of GBR and TDR radial velocity observations together and separately. The relative impacts of assimilating these two ICDR observations are discussed with relevance to their differences in availability and 3D coverage. Hereafter, the acronyms GBR and TDR will be used with the radial velocity observation type being implied.

Hourly DA cycling begins at 1500 UTC October 6 when GBR observations in Matthew's inner core become available. Figure 3.1 shows the initial background horizontal and vertical structure for all experiments, along with GBR observations for the 1500 UTC analysis time overlayed. As a result of limited inner core observations and no VM up to this point, the initial wind field structure is too broad and has only a single wind maximum. Inferring from the reflectivity structure (Figure 2.1A) at this time, Matthew is characterized by concentric eyewalls, which, from previous studies (Willoughby et al., 1982; Houze et al., 2007; Bell et al., 2012) are known to be accompanied by dual wind maxima. In addition to this, its maximum 10 m wind intensity (Vmax) and minimum sea level pressure (MSLP) are too weak compared to the National Hurricane Center's Best Track (BT) (Landsea & Franklin, 2011) estimate by about 32 kts and 23 hPa, respectively. This unrealistic initial storm structure will highlight the cycling system's ability with ICDR observations to make proper corrections to establish CEs. GBR observations cover over half of Matthew's inner core in the horizontal (Figure 3.1A) but have limited lower-level coverage (Figure 3.1B). This is consistent with the discussion in Section 2.3 and distributions shown in Figure 2.4B at this analysis time, where vertical density of GBR observations peaks around 7.5 km AGL in the inner core region.

To illustrate how the GBR observations begin to correct the initially weak and broad vortex, the evolution of the GBR experiment from 1500-1800 UTC October 6 is displayed in Figure 3.2. Cross sections of background and analysis tangential wind are shown with GBR observations represented by black dots and storm relative tangential wind analysis increments contoured every

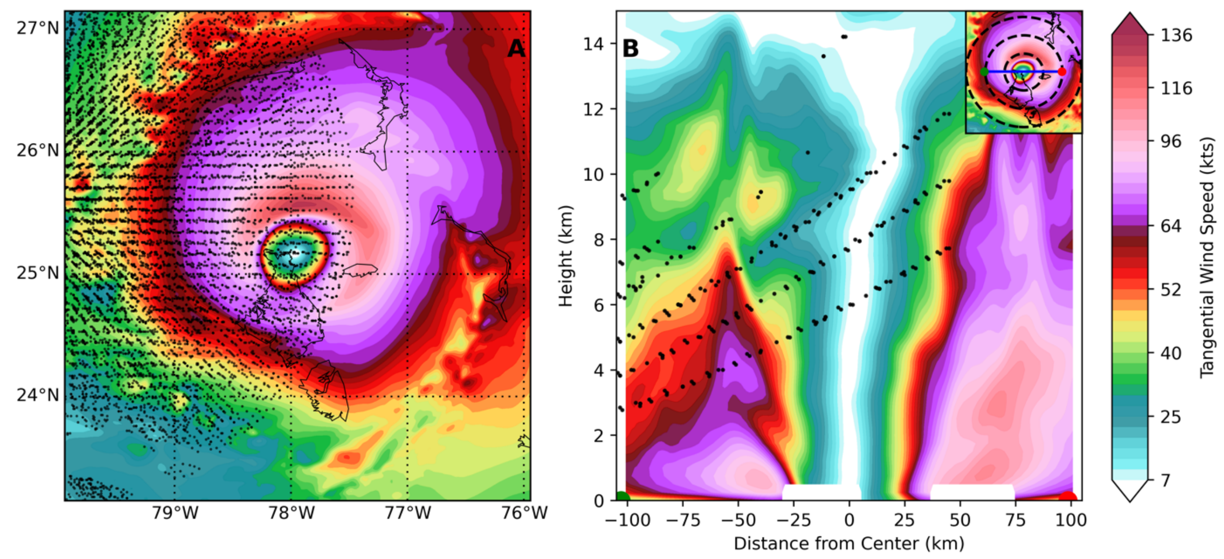

Figure 3.1: Background structure of Matthew at 1500 UTC October 6 before hourly cycling is started. (A) shows horizontal tangential winds at 1km AGL and (B) shows W-E vertical cross section of tangential winds. Observations for the 1500 UTC analysis time are plotted as black dots (all of them shown in (A), while only those within 10 km of the cross section are shown in (B)).

10 kts in black. Positive analysis increments for the tangential wind field at 1500 UTC are maximized in the middle to upper levels, closest to the vertical locations of the observations (Figure 3.2A). These increments initially do not reach the surface due to the vertical covariance localization. The physical result of these increments is to contract and strengthen the tangential wind field in the middle to upper levels while leaving the lower-level wind structure largely intact (Figure 3.2B). Overall, the analyzed wind structure is largely unrealistic after one cycle. However, during the one-hour time integration to the next analysis time, the contracted wind field in the previous analysis's upper levels has extended downward to the surface, leaving a more realistic structure (Figure 3.2C).

Figure 3.2 demonstrates the correction process to the initially inconsistent storm structure when there is a lack of lower-level coverage of ICDR observations during the early cycles. The DA first contracts and/or strengthens the wind field at the middle to upper levels during the DA, followed by the extension of the corrected upper-level winds downward during the time integration, emphasizing the importance of both components of the cycling when vertical coverage from observations is poor. This continues for the next three cycles (Figure 3.2 C-E & E-G) while lower-level coverage of GBR observations slowly improves, allowing for analysis increments to

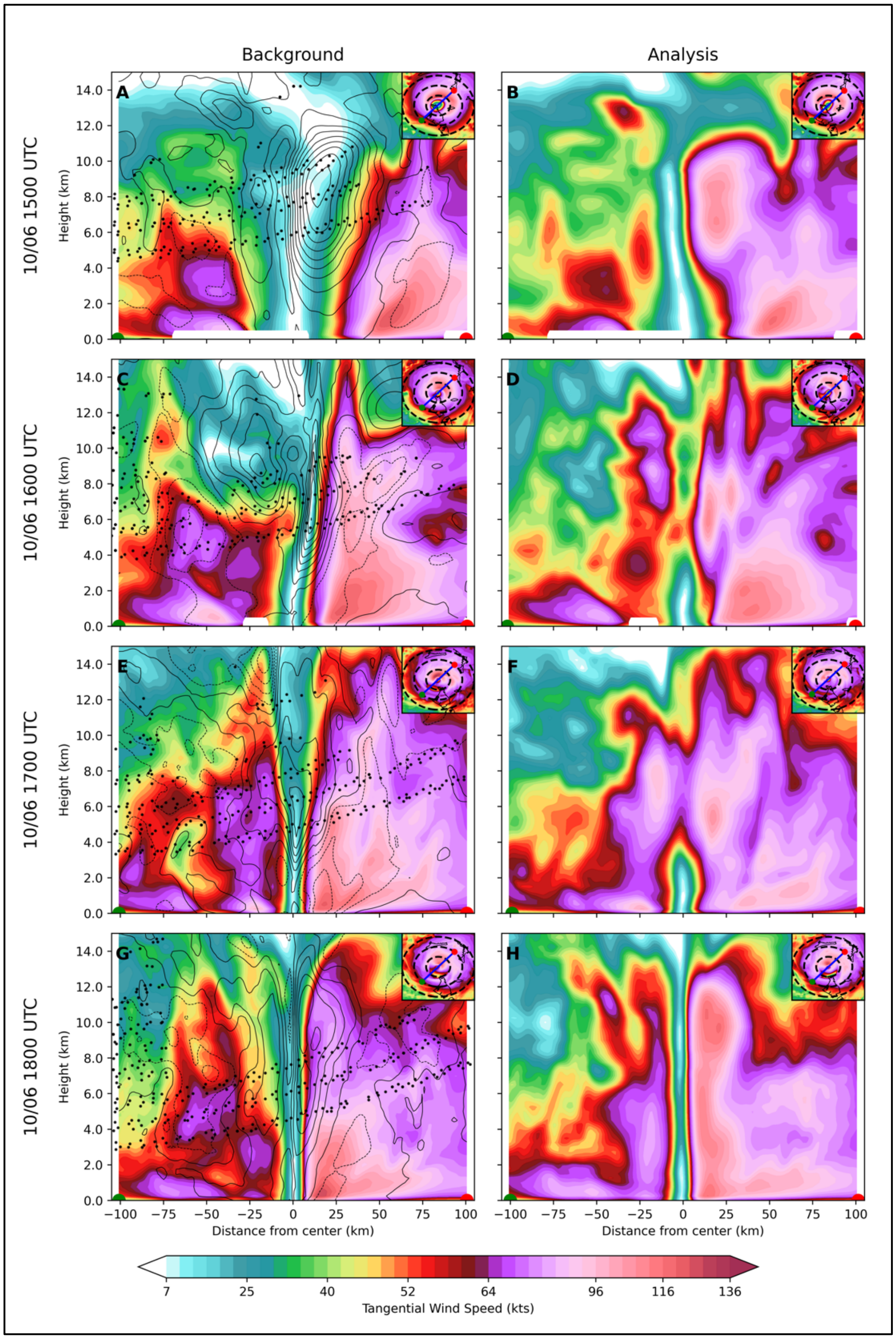

Figure 3.2: Evolution of cross sections from 1500 UTC to 1800 UTC October 6 for GBR experiment. All cross sections are taken at a 45° angle relative to a parallel. Figures in left column show background tangential winds (contour fill), storm relative analysis increments (contoured in black every 10 kts), and GBR observations within 10km of cross section plane. Figures in right column show the analysis tangential wind field.

extend to the surface. At the 1800 UTC analysis time, the first evidence of coherent CE structure is seen in both the background and analysis (Figure 3.2G,H). Figure 3.2H shows primary and secondary wind maxima located around 20-25 km and 50 km from the storm center respectively. Consistent with observational studies (Houze et al., 2007), the primary eyewall is vertically deeper and has no outward tilt with height while the secondary eyewall is shallower and tilts outward with height. The secondary eyewall is an impressive feature for the DA to establish given how vertically shallow it is and the limited vertical observation coverage at the time. With the right side of the cross sections passing through the right-front quadrant of the storm relative to the storm motion, the more intense eyewalls on the right side of the cross section are consistent with expected TC structure. These results demonstrate that continuous, high frequency DA cycling with GBR observations has the ability to establish CE structure, even with limited vertical coverage of the lower levels of the TC.

Relative impacts of assimilating the two different ICDR observations are compared at 1900 UTC October 6. Because this is the first analysis time in which TDR observations are available, it provides the best comparison between the GBR, TDR, and GBTDR experiments to highlight differences between them. These comparisons are done using Figure 3.3 and Table 3.1, but before these are made, some more details about these are given. First, Figure 3.3C-H shows the background and analysis horizontal tangential winds at 3 km AGL for the three ICDR experiments, with storm relative analysis increments contoured in black in the left-hand panels every 10 kts. Figure 3.3A shows the tangential wind calculated from FL RECON zonal and meridional wind observations (black curve), as well as the tangential winds of the experiments. The FL RECON wind profile is time dependent but will be assumed valid at the center fix time of 1917 UTC, which was the closest pass to the 1900 UTC analysis time. The center fix time is the time at which the aircraft passes through the storm center between two penetration legs. The tangential wind profiles for the experiments are obtained by interpolating the 3D tangential wind field to the flight path after the storm has been recentered to the location of the center fix to ensure a fair comparison of structure. For the three ICDR experiments, these paths are approximately represented by the black lines in Figure 3.3C-H. Figure 3.3B shows the 3 km AGL tangential winds from the Hurricane Research Division (HRD) dual doppler wind analysis. It should be noted that the TDR observations are used to create this analysis, so the TDR observations used in the corresponding experiment are not completely independent from the HRD dual doppler analysis. Lastly, Table 3.1 gives the

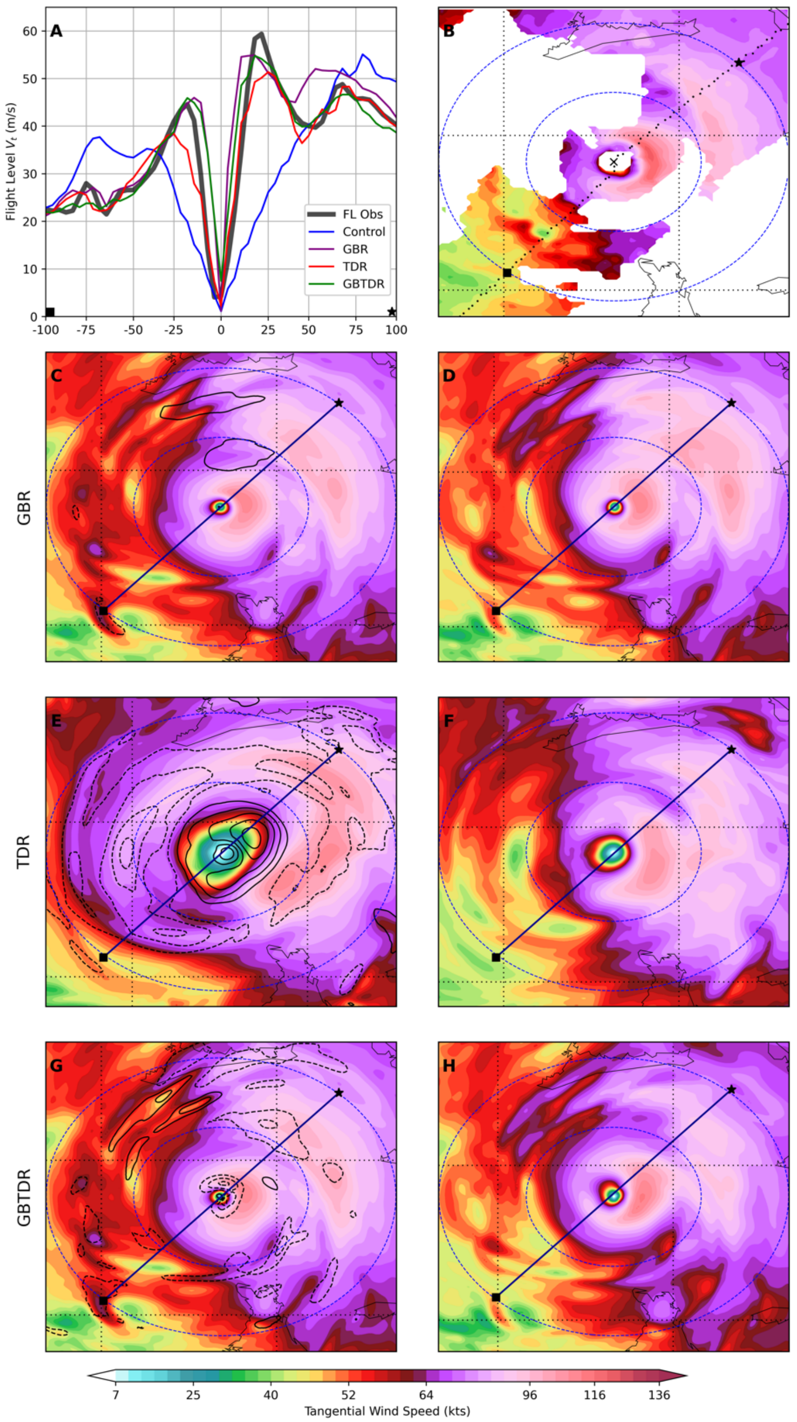

Figure 3.3: Comparison of background (left column, bottom 3 rows) and analysis (right column, bottom 3 rows) 3 km AGL horizontal tangential winds. In background panels, storm relative analysis increments of 3 km AGL tangential wind are contoured every 10 kts with the 0-contour omitted. (A) shows the tangential winds from FL RECON observations along with the tangential wind profiles for the four experiments. (B) shows tangential winds from the HRD dual doppler wind analysis at 3km AGL.

Experiment	**r <= 40 km**	**r > 40 km**	**All r**
Control	0.7735	0.2467	0.8820
GBR	0.9356	0.6215	0.9342
TDR	0.9278	0.8737	0.9315
GBTDR	0.9377	0.7588	0.9347

Table 3.1: Spearman Rank correlation coefficients between 3km AGL tangential winds from HRD dual doppler wind analysis (Figure 3.3B) and 3km AGL analysis tangential wind for each experiment. Correlations are calculated for radii less than or equal to 40 km, greater than 40km, and all radii, to represent the primary eyewall, secondary eyewall, and entire horizontal domain. The largest value for each column is highlighted.

Spearman's rank correlation coefficient between the 3km AGL tangential wind field in each experiment and the HRD dual doppler analysis tangential wind field in Figure 3.3B. The correlation coefficient is calculated for winds in three regions: less than or equal to 40 km in radius, greater than 40km in radius, and for all radii, to approximately represent the correlations of the primary wind maximum, secondary wind maximum, and complete horizontal tangential wind field, respectively.

Starting with the GBR experiment, the magnitude of the analysis increments to the 3km tangential wind (Figure 3.3C) are small compared to the other two experiments (Figure 3.3E,G) and the previous analysis times for this experiment (Figure 3.2). This indicates that the GBR experiment has stabilized, as the large structural changes associated with correcting the initial background have subsided. The small increments to the tangential wind field in the DA update result in no significant changes to the structure in the analysis (Figure 3.3D), with features such as the location and intensity of the two wind maxima being very similar between the background and analysis. Compared to the FL tangential winds, the locations of the primary wind maxima (on both sides of the center) and secondary wind maximum on the right side of the center, are located too far radially inward (Figure 3.3A). In addition to this, the secondary wind maximum on the right side of the center is too strong. Diagnostics suggest that the spuriously small eye is due to the lack of GBR observation coverage at the lower levels. The level of peak coverage of GBR observations is about 7 km AGL according to Figure 2.4B, indicating that the vertical levels containing the most intense winds are not being sampled. Due to this, corrections to the lower-level wind field are made through information spreading via the BEC structure and vertical/horizontal localizations.

TDR experiment has the largest analysis increments to the horizontal 3 km AGL tangential wind field at the 1900 UTC analysis time (Figure 3.3E). The TDR experiment background is similar to the initial storm structure at 1500 UTC, being too broad and only having one primary wind maximum due to the lack of any ICDR observations available up to this point. Figure 3.3E show positive increments inside the area of largest wind gradient associated with the eyewall, which results in a contraction of the wind field to establish a primary wind maximum about 25 km from the center. Negative analysis increments to the tangential wind field are more asymmetric than those in the eye region, occurring at the radius of maximum wind in the west and south parts of the storm, and just inside the radius of maximum winds in the east and north parts. This increment structure diminishes the tangential winds in the west side of the storm and establishes a secondary wind maximum in the northeast side of the storm, which is confirmed in by the tangential wind profile in Figure 3.3A. Compared to GBR and GBTDR, the primary wind maxima are not as intense, and are located more radially outward, however, its position and intensity of the secondary wind maxima is similar to GBTDR and compares favorably to the FL RECON observations.

The GBTDR experiment at this analysis time allows for a direct comparison to the GBR experiment, as the two have identical backgrounds at the 1900 UTC analysis time. With this being the first analysis time in which TDR observations are available, any differences between the GBR and GBTDR analyses can be directly attributed to the addition of TDR observations, allowing for an assessment of the potential benefits of assimilating the two ICDR observations simultaneously. Analysis increments in the GBTDR experiment (Figure 3.3G) are negative inside and at the radius of the primary wind maximum, which is an increment structure consistent with shifting this maximum radially outward. In addition to this, negative increments are located at and just inside the radius of the secondary wind maximum in the northeast part of the storm, which act to weaken the secondary wind maximum in the background as well as shifting it radially outward. These analysis increments differ from the GBR experiment, which suggest the TDR observations are responsible. The differences between the FL profiles in the GBR and GBTDR analyses are seen in Figure 3.3A. The aforementioned deficiencies in the GBR experiment are corrected in the GBTDR experiment, with the location of the primary wind maximum on either side of the center being shifted radially outward, and the secondary wind maximum on the right side of center being weakened and moved radially outward. Both of these changes in the GBTDR analysis update are *more consistent* with the observed FL winds at this time. Correlation coefficients from Table 3.1 confirm that the GBTDR experiment correlates more closely to the HRD dual doppler wind analysis than does the GBR for radii corresponding to the primary wind maximum, secondary wind maximum, and entire horizontal domain. It also correlates the closest to the HRD dual doppler wind analysis for all radii out of the three ICDR experiments. Diagnostics reveal that the corrections to the lower-level wind field are likely due to the increased lower-level coverage from the TDR observations, with peak vertical coverage around 1 km AGL (Figure 2.4D). The horizontal peak coverage is 75 km in radius (Figure 2.4C), as the plane was flying a penetration leg during the DA time window. The TDR's superior 3D observation coverage in this analysis complements the GBR observations, demonstrating one of the benefits of assimilating both GBR and TDR simultaneously for the analysis of Matthew's CE structure, especially when vertical coverage differs drastically between the two types of observations.

The above analysis puts forth some of the benefits and drawbacks of each ICDR observation set. Overall, the TDR experiment demonstrates the ability to correct the initially inconsistent and broad wind structure more quickly than GBR due to differences in vertical coverage of the ICDR observations. However, the GBR experiment shows the advantage of having ICDR observations available earlier and continuously, as it is able to correct Matthew's structure before the TDR observations become available, despite their limited lower-level coverage. At the first analysis time when TDR is available, the GBTDR experiment shows the ability of the GBR and TDR observations to complement each other in terms of their vertical and horizontal observation distributions, as they are directly sampling different parts of the storm.

To assess overall structural evolution of each experiment for the entirety of the cycling from 1500 UTC October 6 to 1500 UTC October 7, a Hovmöller diagram of azimuthally averaged 1 km AGL tangential winds of the model analyses is shown in Figure 3.4. Dashed black curves represent the CFs to the FL RECON wind radius observations in Figure 2.2A. It should be noted that because these observations are coming from FL (approximately 3 km AGL), the radius representing the primary eyewall will be more representative of its location at 1km AGL than the radius representing the secondary eyewall due to its tilt with height. Black dots indicate local maxima in the azimuthally averaged wind field at each analysis time. Blue dashed lines indicate the bounds

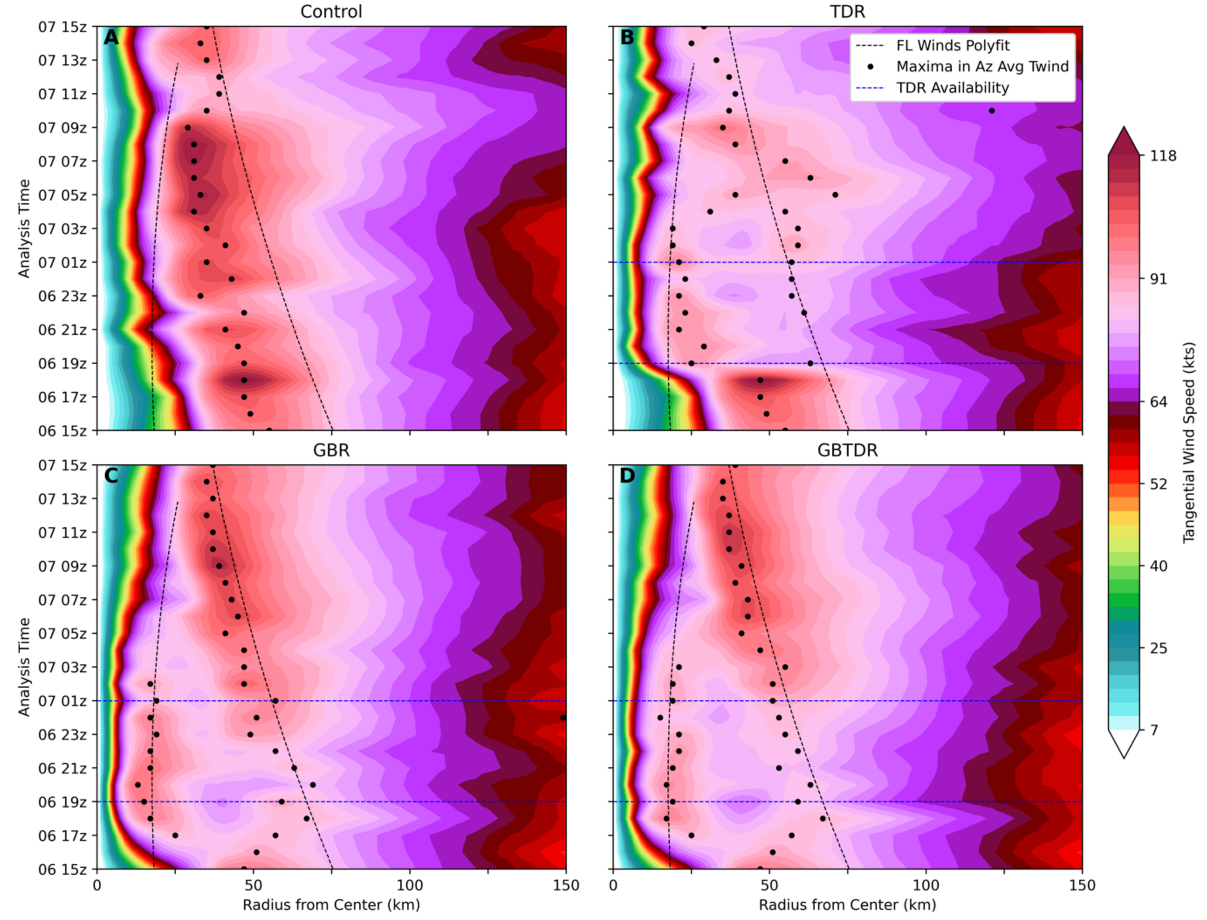

Figure 3.4: Hovmöller diagrams of azimuthally averaged tangential wind at 1km AGL for the analyses in the four different experiments. Black dots indicate local maxima in the azimuthally averaged tangential wind field. Dashed black line represent the CFs to the FL RECON wind observations radius data from Figure 2.2A as additional aid for identifying approximate locations of the primary and secondary wind maxima throughout the cycling times. Blue horizontal dashed lines represent the bounds of TDR availability, which are displayed on each of the three ICDR experiments' panels.

of the TDR availability for the three ICDR experiments. Throughout the 24-hour period of cycling, Control shows no ability to establish CE structure, or to accurately represent the structural changes associated with the evolution of the ERC. This demonstrates that without any ICDR observations, the kinematic structure cannot be corrected through DA cycling. In contrast to the Control, the GBR and GBTDR experiments (Figure 3.4C,D) are able to correct the initial background by establishing dual wind maxima by 1800 UTC October 6, consistent with the evolution of analyses in Figure 3.2, with primary and secondary wind maxima located around 20 and 70 km respectively in the azimuthal average. Subtle differences exist between the 1km azimuthally averaged wind structure between GBR and GBTDR throughout the rest of the cycling and ERC evolution. The GBR experiment has a tendency to pull the primary wind maximum too far radially inward (Figure 3.4C) for several analysis times in the 1800 UTC to 0200 UTC time period, whereas the GBTDR has a tendency to keep the local maximum inside the CF. In addition to these differences, the GBR establishes a stronger secondary wind maxima associated with the reintensification phase earlier than in GBTDR (e.g. 2300 UTC October 6). This difference takes place in the period of TDR cycling, suggesting that the weaker azimuthally averaged winds associated with the secondary eyewall in the GBTD experiment are tied to the addition of the TDR observations. The strengthening and contraction of the secondary wind maxima in these two experiments are similar and consistent with the reintensification phase of the ERC. Both the GBR and GBTDR have similar contraction rates and radial locations of the secondary wind maximum. Differences in the decay of the primary eyewall between these two experiments are small, with the GBTDR showing the primary eyewall having an established local maximum in the azimuthally averaged wind field for one hour longer than GBR. Overall, without having knowledge of the entire 3D kinematic structure of the observed storm for the entirety of the cycling time, it is difficult to identify which of the two experiments is more realistic. However, while benefits of TDR were shown to be complementary to the GBR observations in terms of lower-level coverage at 1900 UTC October 6, the addition of the TDR to the GBR does not drastically change the azimuthally averaged structural evolution throughout the 24-hour cycling time in the GBTDR experiment, at least at the lower levels.

Examining the TDR experiment, the establishment of dual wind maxima, as discussed previously, does not occur until the 1900 UTC October 6 analysis time, where before that, only a single wind maximum is analyzed identical to the control (Figure 3.4B). After this time, dual wind maxima are established in the azimuthal mean, evidenced by multiple local maxima in the field. However, the placement and evolution of both azimuthally averaged wind maxima are more poorly represented than in GBR and GBTDR for the rest of the cycling. The evolution of the ERC as represented by the TDR experiment does not properly represent the contraction and strengthening associated with the reintensification phase, which the GBR and GBTDR successfully capture. These deficiencies in the TDR analyses are hypothesized to result for two reasons. The first is that the TDR observations become available later and become unavailable earlier compared to GBR observations, which allows for less time to make corrections to the initially inconsistent storm

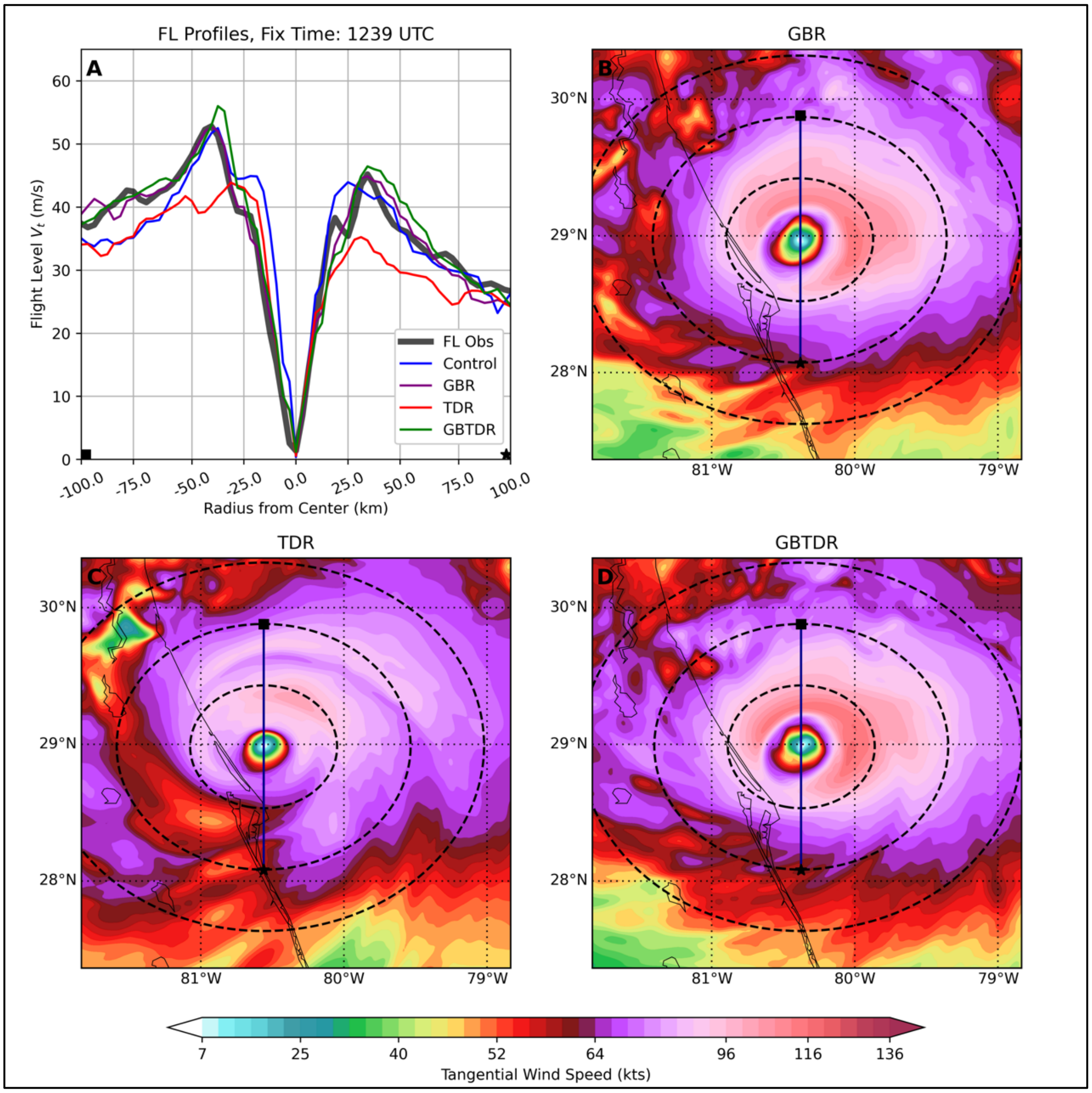

Figure 3.5: (A) FL RECON tangential winds (1239 UTC October 6) and tangential wind profiles (1300 UTC October 6) as in Figure 3.3A. 1km AGL horizontal tangential wind for the three ICDR experiments is plotted in panels B-D. Range rings are plotted as dashed black lines every 50km. The vertically oriented black line represents the location of the FL RECON observations and location of the tangential wind profiles for the experiments. The flight path direction is southward, with the black square and black dot on the horizontal plots and tangential wind profile plots helping with orientation.

structure. The second is the inconsistent horizontal coverage of TDR observations from analysis time to analysis time (Figure 2.4C). When TDR observations in the DA time window are taken from a downwind flight leg, the analyses are expected to be less accurate due to incomplete sampling, which can then carry over to the following analysis times. The TDR, however, does offer improvements over the Control during the time frame when observations exist by displaying ability to establish CE structure. Comparison of the TDR with the GBR or GBTDR experiments highlights the importance of continuous DA cycling with GBR observations by the superior structural evolution in the GBR and GBTDR experiments. The earlier availability of GBR observations results in a faster correction to establish CE structure, and longer duration of coverage results in the correct evolution of the storm structure during the reintensification phase.

To further expand on the effects of the lack of continuous cycling of ICDR observations after the cease in TDR observation availability, 1km tangential wind analyses and FL RECON tangential winds are shown in Figure 3.5 for the three different ICDR experiments at 1300 UTC October 7, near the end of the ERC. Note that the FL RECON fix time was at 1239 UTC, which happens to be the closest to the analysis time. Consistent with Figure 3.4, the GBR and GBTDR analyses have well established, strong wind maximum that correspond to FL observations closely in both strength and intensity (Figure 3.5A). This single eyewall (originally the secondary eyewall) is now the prominent feature in the analyses after its contraction and strengthening throughout the reintensification period. The TDR experiment is visually weaker in intensity of its eyewall (Figure 3.5C) which is verified by the FL RECON tangential winds, with its wind maximum about 10 m/s weaker than FL RECON on either side of the cross section. Its maximum wind on either side is also located too far radially inward. These results again emphasize the importance of having continuous access to ICDR observations when the structure of the inner core is rapidly changing. The GBR and GBTDR also begin to assimilate GBR observations at lower levels throughout the rest of the cycling after TDR observations cease (Figure 2.4B). The consecutive cycling with continuous GBR access also will provide benefits for the forecasts of the ERC, which is the focus of the next section.

3.2 Forecasted Structure and Intensity Changes throughout Matthew's ERC

The focus of this section now switches to the structural and intensity forecasts for Matthew's ERC initialized from the analyses discussed in Section 3.1. The forecasted kinematic structure of all deterministic free forecasts is explored using Hovmöller diagrams and verification against independent GBR observations. Variability in the forecasts between analysis times are also discussed. Intensity forecasts of Vmax are shown to determine if forecasted ERCs have consistent changes in both single point intensity (Vmax) and structure during the weakening and

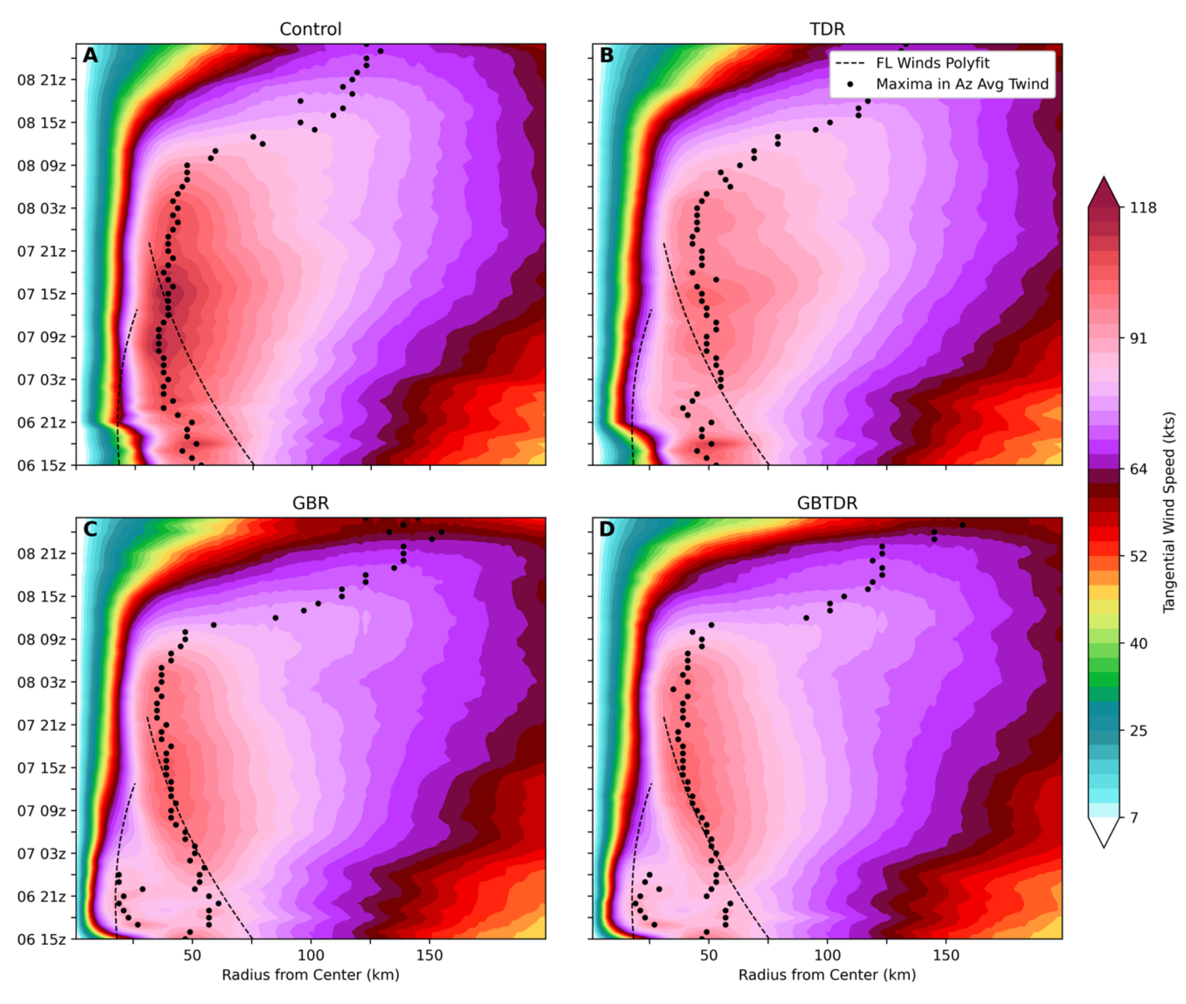

Figure 3.6: Time average for all deterministic free forecasts for 1km AGL azimuthally averaged winds. To obtain the time average at each date, the field from any analysis or forecast valid at that date is averaged over. This will mean that each date will have a different number of valid forecasts/analyses to average over. Dashed black curves are CFs to the FL RECON wind observations radius data from Figure 2.2A. Black dots represent local maxima in the time averaged field at each date.

reintensification phases as documented systematically by Sitkowski et al. (2011). Lastly, the mechansim for the decay (stregnthening) of the primary (secondary) eyewalls are briefly discussed in terms of balanced and unbalanced dynamics in an axisymetric framework.

Due to the large number of forecasts from 24-hours worth of cycling for the four experiments, the resulting strucutral forecasts from 1500 UTC October 6 to 1500 UTC October 7 are sumarized in Figure 3.6. The y-axis represents the average of a field (in this case 1km AGL azimuthally averaged tangential winds) over any free forecast/analysis valid at each date. For example, at 1600

UTC October 6, the 1-hour forecast from the 1500 UTC October 6 forecast, and the 1600 UTC October 6 analysis would be used to calculate the average. This results in the dates having a different amount of "data points" to average over, with the earlier dates in the cycling period having less than the later dates. This method was determined to be the best way to highlight overal forecasted structre for the large amount of forecasts. These averages will be reffered to as "time averages" for each date, which are displayed in Hovmöller format. Similar to Figure 3.4, the black dots represent local maxima in the time averaged field at each date. In the time average, the Control is unable to capture the correct structural changes associated with the weakening and reintensification phases of the ERC (Figure 3.6A). This is a direct result of the Control's inability to accurately analyze Matthew's CE structure throughout the cycling as discussed in Section 3.1 and highlights the importance of proper initialized TC structure using inner core doppler radar observations for the resulting forecasts.

The time average from TDR forecasts (Figure 3.6B) show the lack of *continuous* ability to predict the correct structural changes of the primary and secondary eyewalls during the ERC. After the 1900 UTC October 6 analysis time when TDR observations become available, the time averaged tangential winds begin to contract inward, closer to the CF for the primary eyewall, which is a result of four consecutive cycles (not shown) whose forecasts demonstrate the expected structural changes for the ERC. Overall, a majority of the TDR forecasts do not show the correct structural changes associated with ERC, and as a result of this, clear maxima representing the primary eyewall in the time average are not seen. After 0200 UTC October 7, the time average registers maxima that would correspond to the secondary eyewall's contraction and strengthening. However, on average, the contraction rate is not fast enough compared to the CF. The unrealistic time averaged forecast structure in the TDR experiment is likely a result of the inaccurate structure (relative to the GBR and GBTDR) in the analyses as discussed in Section 3a in relation to Figure 3.4C. The limited temporal availability of TDR and the changes in the horizontal observation distribution relative to the storm center are hypothesized to be the cause of the inaccurate forecast structure. It is important to note that the time averaged structural forecasts are not representative of all forecasts during the cycling, and an example of a more realistic forecast from TDR is shown later in the section. Despite the lack of consistent and continuous ability to correctly forecast the structural changes associated with the ERC, the TDR experiment does show improvements over the Control experiment. This is due to its ability to capture the realistic evolution of the concentric eyewalls during the four aforementioned forecasts during ICDR observation availability.

In contrast to the Control and TDR experiments, the GBR and GBTDR experiments show superior ability in capturing the primary and secondary wind maxima in their forecasts. Primary wind maxima are captured as distinct local maxima in the time averages from 1700-0000 UTC indicating the forecast of the primary eyewall and its decay are happening consistently during the forecasts. The secondary wind maxima in the time average for the GBR and GBTDR experiments are very similar, with small differences in radial position occurring at times, but with both experiments having very similar contraction rates in the time average. Overall, the forecasted secondary eyewall for these two experiments replaces the primary eyewall at a radius greater than suggested by observations, however, they are more accurate than in Control and TDR. The superior analysis structure of the GBR and GBTDR experiments in Figure 3.4C,D result in consistent structural forecasts to be made earlier, starting at 1600 UTC (not shown), and more frequently, accounting for the time averaged forecasts capturing both the primary and secondary eyewall evolutions consistently throughout the cycling.

To provide quantitative verification of forecasted structure in the different experiments, root mean square differences (RMSD) between GBR radial velocity observations and the forecasts are calculated. Note that at the analysis time (forecast lead time 0), GBR radial velocity observations and the GBR/GBTDR experiments will not be independent. Before the RMSDs are calculated, the forecasted TC is relocated to its observed location at each forecast time, this way the RMSD values will be more representative of structural differences with no contributions from track error. The RMSD values are averaged for each lead time and are shown in Figure 3.7. Results from the GBR and GBTDR confirm the qualitative findings from Figure 3.6, having smaller RMSD values than Control and TDR for all forecast lead times shown. As expected, the RMSD values for GBR and GBTDR at forecast lead time 0 (analysis time) are much lower than the other two experiments, as the GBR and GBTDR experiments assimilate these observations and they are not independent. The small averaged RMSD value around 3.2-3.3 m/s is consistent with the observation error for GBR observations used during DA, indicating the DA is performing correctly. The RMSD values for TDR show that at the analysis time, on average, its analyzed structure is better than the Control's, as discussed in Figure 3.4. However, at many lead times, the Control has a better average RMSD value than TDR, which is likely due to consistency of the Control's forecasted single

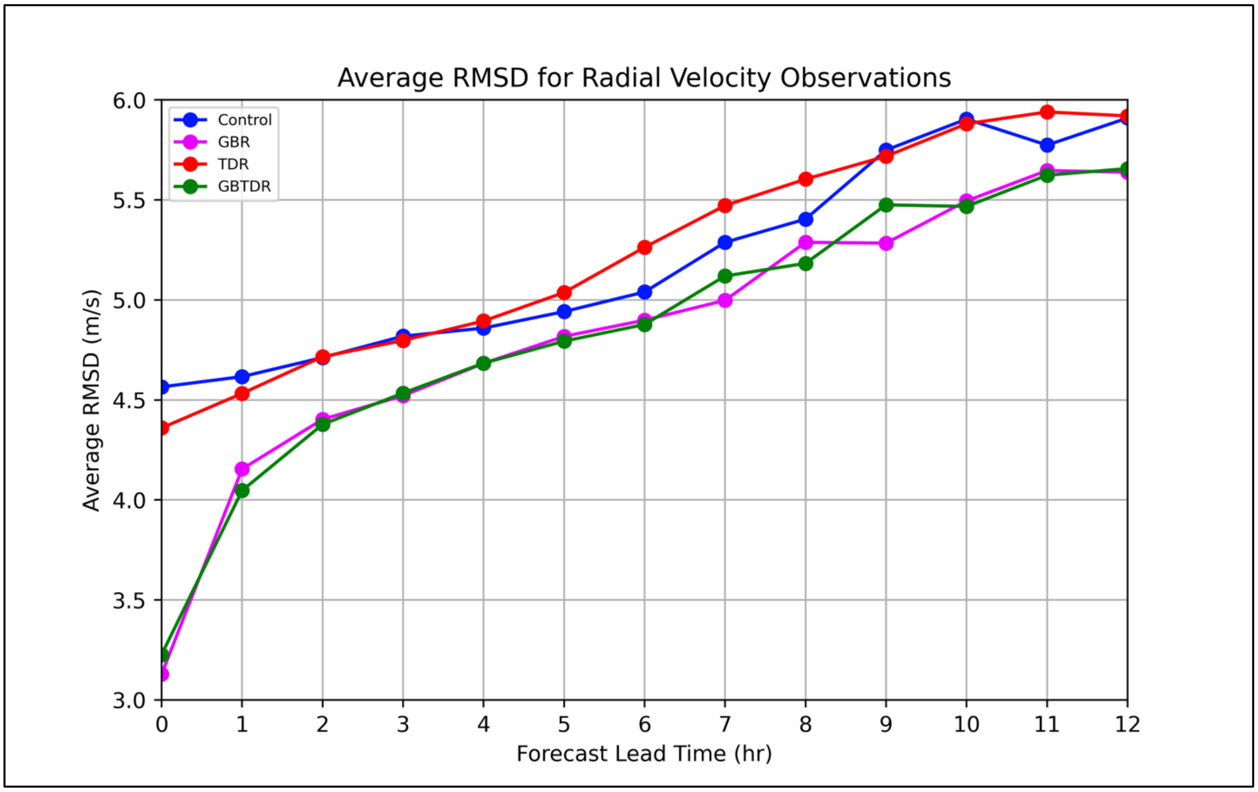

Figure 3.7: Root mean square differences (RMSD) between GBR radial velocity observations and radial velocity of the experiments using the coastal radars KAMX, KMLB, and KJAX. RMSDs are averaged for each lead time.

eyewall's location in relation to its observed location. Figure 3.6 shows the time averaged forecasted wind maxima for Control lies closer to the observed location than does TDR at the end of the ERC, but has no physical significance given the Control's inability to analyze and forecast the structure correctly for any analysis time throughout cycling. On average, the consistent structural forecast from select TDR cycles is overwhelmed by the more frequent poor forecasts.

Figures 3.6 and 3.7 do not account for the variability in the free forecasts from analysis time to analysis time. To demonstrate the variability in the forecasted structure, Hovmöller diagrams of 1km azimuthally averaged tangential wind at the 1900 UTC October 6 and 0000 UTC October 7 analysis times are shown in Figure 3.8. Several features in the forecasts vary, including the location of the eyewalls, the time it takes for the primary eyewall to decay, the contraction rate of the secondary eyewall, and the strength of the secondary eyewall after completion of the ERC. At the 1900 UTC analysis time, the Control, as discussed previously, does not have a correctly initialized structure and produces a forecast with only a single eyewall for its entirety. The three ICDR experiments, however, all have primary and secondary eyewalls present in their forecasts. The

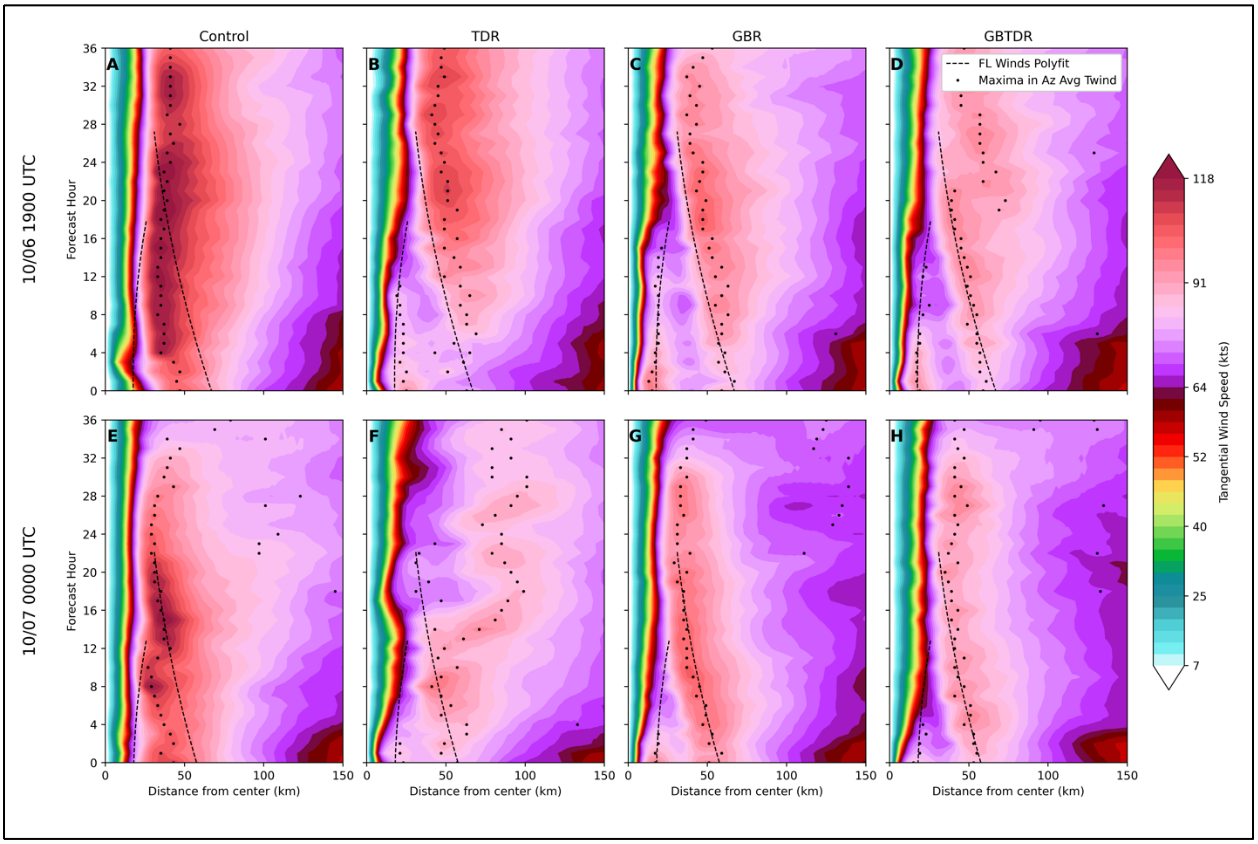

Figure 3.8: Hovmöller diagrams of 1km AGL azimuthally averaged tangential winds for 1900 UTC October 6 and 0000 UTC October 7. CFs and black dots are same as in Figures 3.4 & 3.6.

primary eyewalls decay after some time while the secondary eyewall strengthens and contracts, however, each of the ICDR experiments have differences in their evolutions. The primary eyewall takes the longest time to decay in the GBR experiment, followed by GBTDR and TDR, with the GBR also having the strongest initialized primary eyewall in terms of its azimuthal average. Out of the three ICDR experiments, the TDR has the strongest and most broad secondary eyewall at the end of the ERC, followed by GBR and GBTDR. Interestingly, the GBTDR experiment shows signs of another ERC starting around forecast hour 20 but is not observed. The experiment with the best contraction rate is GBTDR, with the GBR and TDR having slower contraction rates, and secondary eyewalls occurring more radially outward compared to GBTDR. An apparent distinction between the TDR and other two ICDR experiments is the less pronounced secondary eyewall initially in the azimuthal average (Figure 3.8B, forecast hour 0). Horizontal cross sections at this time (not shown) indicate that a secondary eyewall is present but does not cover the same azimuthal extent as do GBR and GBTDR, and it is also more asymmetric, which causes a local maximum in the azimuthal average to not be as clear. This is consistent with the discussion about more inaccurate analyses of the TDR and their effects on the subsequent forecasts.

At the 0000 UTC October 7 analysis time, the TDR experiment stands out between the three ICDR experiments, as it does not show the correct structural changes associated with the ERC as it did at 1900 UTC October 6. A clear contraction of the secondary eyewall is not seen, with periods of contraction and expansion both present in the forecast. These changes are in part due to the vortex structure oscillating between an elliptical and annular shape which changes the projection of the wind field onto the azimuthal mean. However, this does not completely account for the inconsistent evolution seen in the Hovmöller diagram. After further inspection of the evolution of horizontal winds at 1km (not shown), it is clear that this forecast does not show consistent changes with an ERC. The result is a broad, annular TC with radius of maximum winds just inside 100 km by the end of the ERC, more than half of the radius of the eyewall in the GBR and GBTDR forecasts. This forecast is one example of the aforementioned poor forecasts produced by the TDR that degrade the time averaged forecast structure in Figure 3.6. At this analysis time, unlike the 1900 UTC October 6 analysis time, poor horizontal observation coverage is seen in Figure 2.4C, indicating the flight was in a downwind leg during the DA time window. Horizontal tangential winds at 1 km AGL for this analysis time (not shown) reveal less robust secondary and primary eyewall, which is reflected by the intensity of the azimuthally averaged winds at the analysis time compared to GBR and GBTDR (Figure 3.8 F,G,H). The less robust wind maxima initialized in the TDR analysis would cause differences in the evolution of the ERC.

The GBR and GBTDR forecasts at the 0000 UTC October 7 analysis time again have initialized primary and secondary eyewalls that are well represented in the azimuthal average and show consistent structural changes with the decay of the primary wind maxima and contraction/strengthening of the secondary wind maxima. Contraction rates between the two are very similar, and the GBR has a better position of the secondary wind maxima (just inside the CF). The primary eye in GBR again is initialized stronger than in GBTDR and takes longer to decay. The secondary eyewall in GBR also ends up being more intense at the end of the ERC than GBTDR. This consistency in the GBR and GBTDR forecasts to make more accurate structural forecasts is the reason for the distinct primary and secondary eyewall forecasts that manifest themselves in the time average in Figure 3.6.

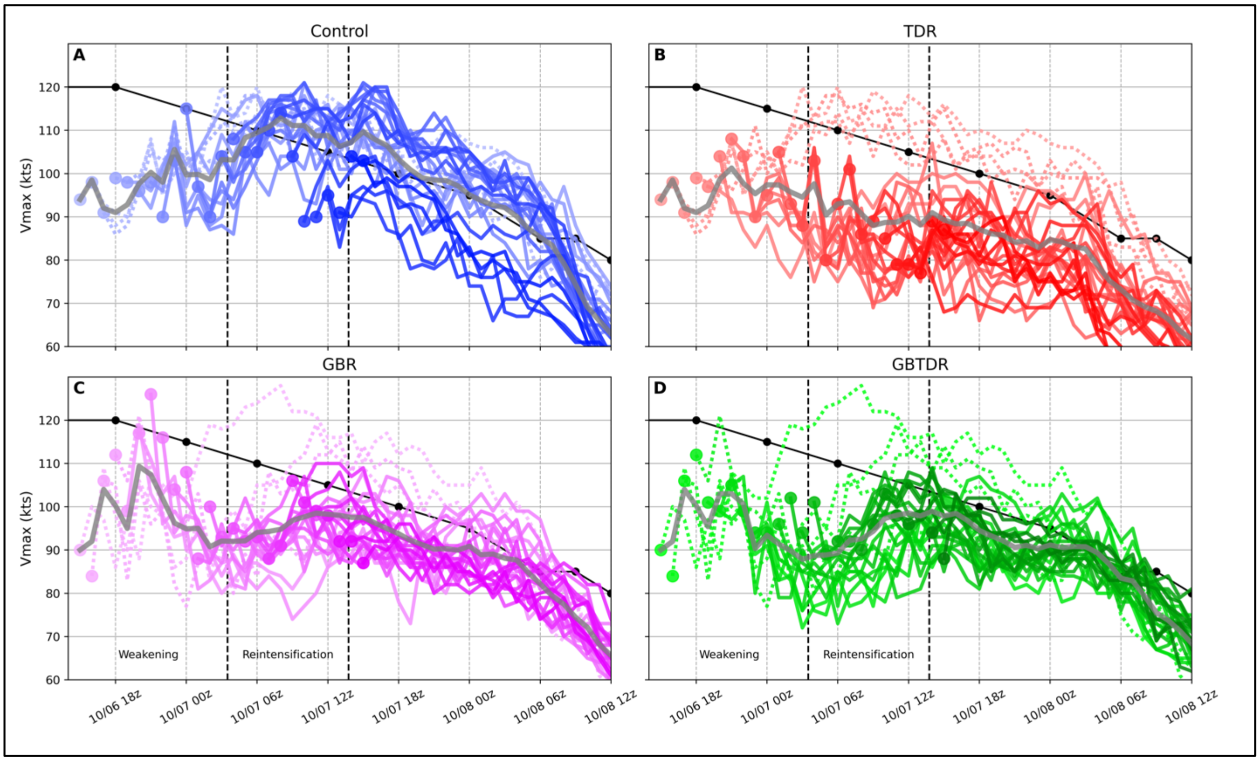

Figure 3.9: 10m maximum wind speed (Vmax) for all free forecasts from 1500 UTC October 6 to 1500 UTC October 7. Dotted lines represent free forecasts initialized before 1900 UTC October 6. Each intensity forecast is marked with a dot at the analysis time to track how the analysis Vmax evolves. Grey curve represents time average of all analyses/forecasts valid at each date. Black line with dots is the BT for Matthew. Vertically dashed black lines represent the bounds of the different ERC phases from FL observations (Figure 2.2) which are labeled at the bottom of panels C & D, with the last vertical line representing the end of the ERC.

The associated intensity changes of the free forecasts are now discussed to determine whether they are consistent with the structural changes presented in Figures 3.6,3.7, & 3.8. Figure 3.9 shows line plots representing all Vmax intensity forecasts during the consecutive cycling with the dots representing the Vmax value at each analysis time. The dashed Vmax forecasts for each experiment are free forecasts from 1500-1800 UTC October 6. For GBR and GBTDR experiments, this time frame represents the period of large structural changes during the DA cycling displayed in Figure 3.2, while for TDR this time period corresponds to analysis times having no TDR observations. For the three ICDR experiments, these analysis times produce the most volatile intensity changes and most intense forecast at later lead times. The time average of the Vmax forecasts using the same method as in Figure 3.6 are displayed as grey lines which help to identify overall trends in the forecasts. The black line in each represents the BT maximum sustained winds, which shows a general weakening trend throughout the rest of Matthew's lifetime. Vertical dashed lines indicate the times at which the ERC changes from the weakening to reintensification phases, and the end of the ERC, as in Figure 2.2.

The intensity forecasts from the Control experiment are largely consistent with the mean structural changes in Figure 3.6A. The time mean of the intensity guidance shows a general strengthening trend up to around 0700 UTC October 7 which matches the increase in mean intensity from the 1km wind forecasts in Figure 3.6A. Given the initial discrepancy of Vmax in the Control experiment compared to the BT, the slow and steady increase in intensity during cycling represents the inability for the DA to correct the initial intensity and structure of Matthew quickly, as no ICDR observations are provided to Control.

In direct comparison to the Vmax forecasts in Control, the GBR and GBTDR forecasts and time mean show four different phases with subtle intensity changes. These phases will be discussed for the GBR experiment, with a corresponding comparison for GBTDR that follows. In addition, the intensity trends will be related to the structural changes in Figure 3.6. From 1500 UTC to 2000 UTC October 6, the GBR displays a strengthening trend as shown by the time mean and purple dots representing the analysis Vmax. At 2100 UTC October 6, the Vmax in GBR is strengthened to about 125 kts, about 7 kts stronger than what Best Track suggests at the time. This period of intensification in the analyses and forecasts represent the adjustment of the initially weak vortex through the continuous DA cycling using GBR observations. This is consistent with the structural changes in Figure 3.6C, where the establishment of two wind maxima is taking place as evidenced by two local maxima in the time mean. Following this strengthening, a weakening trend from 2000 UTC October 6 to 0200 UTC October 7, followed by a strengthening trend from 0200 UTC to 1100 UTC October 7. We will argue in the discussion to come that these two periods of different intensity trends are a result of the free forecasts correctly capturing the weakening and reintensification phases of the ERC. From 2000 UTC October 6 to 0200 UTC October 7, the time mean of GBR forecasts in Figure 3.6C show the weakening of the primary wind maxima and the strengthening of the secondary wind maxima associated with the weakening phase of the ERC, in which the maximum wind will still be located in the primary eyewall. From 0200 UTC to 1100 UTC October 7, the secondary eyewall in the time mean of the forecasts (Figure 3.6C) becomes stronger than the primary eyewall, and begins to intensify while it contracts. Lastly, after 1100 UTC October 7, the intensity trend switches to deintensification associated with deteriorating environmental conditions after the ERC is complete, which is also consistent with the mean structural forecasts in Figure 3.6C. Overall, the intensity trends shown for GBR in Figure 3.9 are consistent with the structural forecasts in Figure 3.6 & 3.7.

Although similar intensity trends from the forecasts in GBR and GBTDR are seen in Figure 3.9, there are a few notable differences. First, the intensity of the GBTDR analyses does not reach that of GBR, with the addition of the TDR observations at 1900 UTC October 6 keeping the GBTDR experiment from further strengthening. Another difference is the timing of the intensity trend changes, with the GBTDR switching from the weakening to reintensification phase, as well as from the reintensification to final weaking phase (after ERC completion) later than did the GBR. The intensity changes in Figure 3.9D match the structural changes in the time mean of the GBTDR forecasts in Figure 3.6D, as in the GBR experiment.

The TDR intensity forecasts in Figure 3.9 do not show these aforementioned subtle intensity trends seen in GBR and GBTDR. This is consistent with discussion of the time mean TDR forecasts (Figure 3.6B), with only a few forecasts being able to successfully capture the correct structural changes with the weakening and reintensification of the ERC. As excepted, the corresponding intensity changes are not captured in the time mean of the Vmax forecasts (Figure 3.9B). The four individual forecasts, however, that do capture the correct structural changes, (Figure 3.8B is an example) show the same intensity trends discussed for the GBR and GBTDR experiments. Unlike GBR and GBTDR, the adjustment of the initial vortex in the DA cycling is not as drastic. Again, the TDR demonstrates its inability to make *consistent* forecasts of the appropriate intensity changes associated with the evolution of the ERC, unlike the GBR and GBTDR.

The claims made arguing that the intensity trends from the GBR and GBTDR free forecasts are consistent with structural changes in the weakening and reintensification phase of the ERC are examined by considering the 1900 UTC October 6 free forecast from the GBTDR experiment in Figure 3.10. The left panel of this figure shows a Hovmöller diagram of the 10 m azimuthally averaged tangential wind with black dots corresponding to local maxima in the azimuthal average and black horizontal dashed lines representing the observed bounds of the ERC phases. The right panel shows a scatter plot of the Vmax intensity forecast for this analysis time. The color of the dots corresponds to the radial distance from the storm center that the Vmax value was found. The coloring strategy is used to identify if the Vmax value is coming from the primary wind maximum (blue, or inside 25 km) or the secondary wind maximum (red, or outside 25 km). Overlayed on the

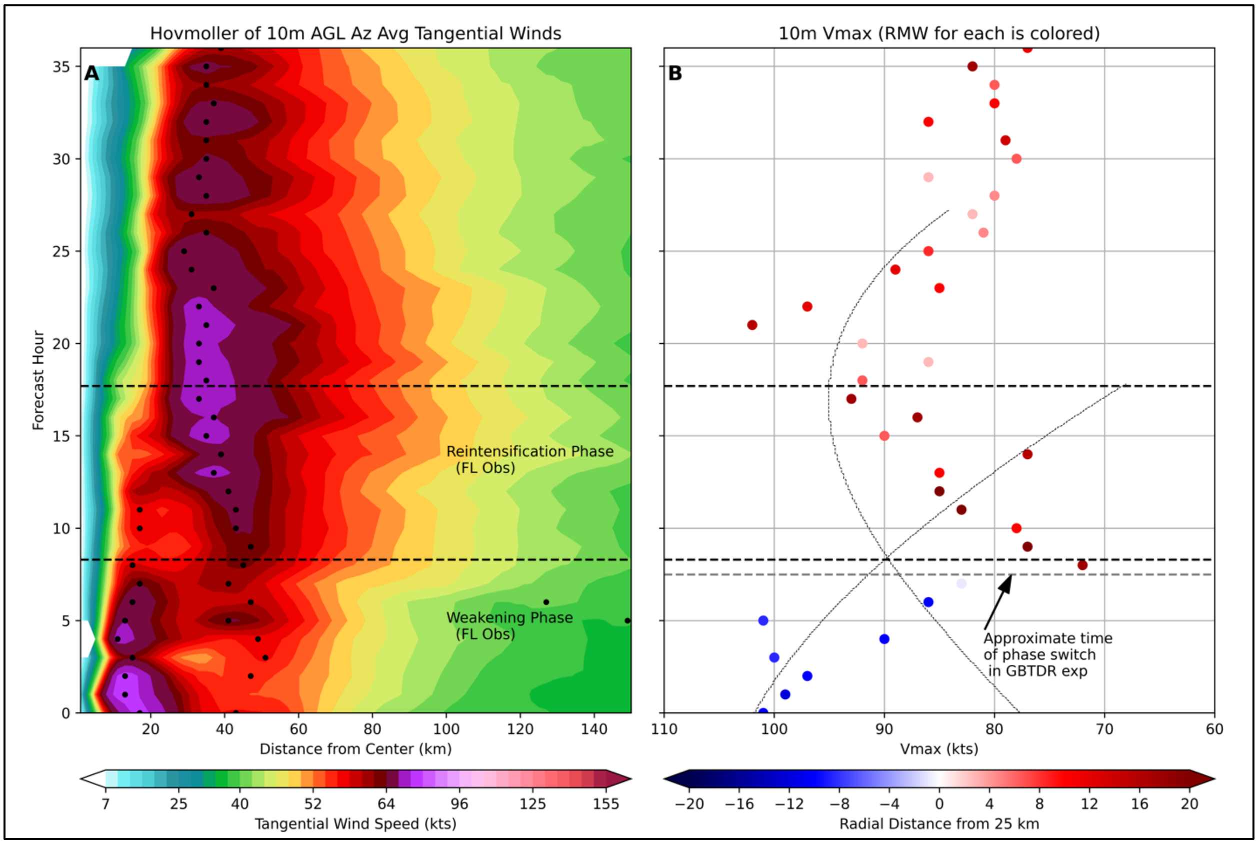

Figure 3.10: Hovmöller diagram from GBTDR experiment initialized at 1900 UTC October 6 of azimuthally averaged 10m tangential winds (A) and corresponding scatter plot of Vmax forecast with colors corresponding to radial distance from 25km from storm center (B). The dashed curves in (B) represent the CFs to the wind maximum of the primary and secondary eyewalls from Figure 2.2 to show intensity trends. Black horizontal dashed lines indicate the observed phase changes in the ERC as in Figure 2.2.

scatter plot are the CFs from Figure 2.2 for the primary and secondary eyewalls. The purpose of these curves is to show *when* the intensity changes occur during the different phases, along with the intensity trends associated with them. They are not meant to be a proxy for intensity, since the observations used to derive the CFs come from FL (about 3 km AGL) while the Vmax values come from 10 m AGL.

For the first 7 hours of the forecast, the Hovmöller shows the primary eyewall as the dominant feature, with the secondary eyewall being noticeably weaker (Figure 3.10A). During this time, the Hovmöller shows the azimuthally averaged 10 m wind intensity becoming gradually weaker, with a brief uptick in intensity around forecast hour 4-5. The scatter plot (Figure 3.10B) shows the decreasing trend in intensity and verifies that the radii at which the wind maxima are occurring are inward of 25 km (blue) which correspond to the primary eyewall. This weakening of the primary eyewall, while still being the stronger of the two, is typical of the weakening phase of the ERC, and is captured in both the point intensity forecast (Vmax) and in structural changes in the Hovmöller. The switch from the weakening phase to the reintensification phase happens sometime between forecast hours 7 and 8, as denoted by the grey horizontal dashed line (Figure 3.10B) and occurs about an hour earlier than indicated by the CFs of the FL wind maxima. Leading up to this time, the secondary wind maximum in the Hovmöller diagram can be seen intensifying and contracting. At forecast hour 8, the secondary wind maximum has now overtaken the primary wind maximum in intensity, as evidenced by the color of the intensity markers in the scatter plot (Figure 3.10B) turning a darker red. This indicates the Vmax values are now located around 40-45 km in radius, consistent with the location of the secondary wind max represented by the azimuthal averaged tangential winds at this time (Figure 3.10A). The forecasted Vmax begins to intensify up to forecast hour 21, with all Vmax values located in the secondary eyewall (red), consistent with the contraction and intensification of the secondary eyewall in the azimuthal mean. The downward trend in intensity after forecast hour 21 is associated with the weakening caused by environmental conditions, again consistent with the Hovmöller's evolution as the azimuthally averaged winds in the eyewall start to weaken.

The relationship between the structural changes seen in the Hovmöllers and the point intensity forecasts demonstrate the model's capability to capture both, consistent with systematically documented structure/intensity changes during the weakening and reintensification phases of the ERC. Given that the Vmax value can be found at any point horizontally in the TC, and ideal forecast capturing the intensity changes associated with these phases would show a pattern consistent with the *maximum value* of the two CFs of wind intensity. The example shown in Figure 3.10 demonstrates that this is the case, and that these intensity changes match what would be expected given the structural changes in the Hovmöller. Because these changes are tied to the evolution of the decay of the primary eyewall and strengthening/contraction of the secondary eyewall, capturing these subtle intensity changes will help signal the oncoming changes to the TC's wind structure, which is impactful for forecasting implications.

To demonstrate that the intensity/structural changes discussed in Figure 3.10 occur for more than just one forecast for the GBTDR experiment, Vmax forecasts for each experiment are scattered using the same methodology in Figure 3.10B. These are shown in Figure 3.11. Only experiments initialized after 1800 UTC October 6 are considered, as the experiments in the 1500

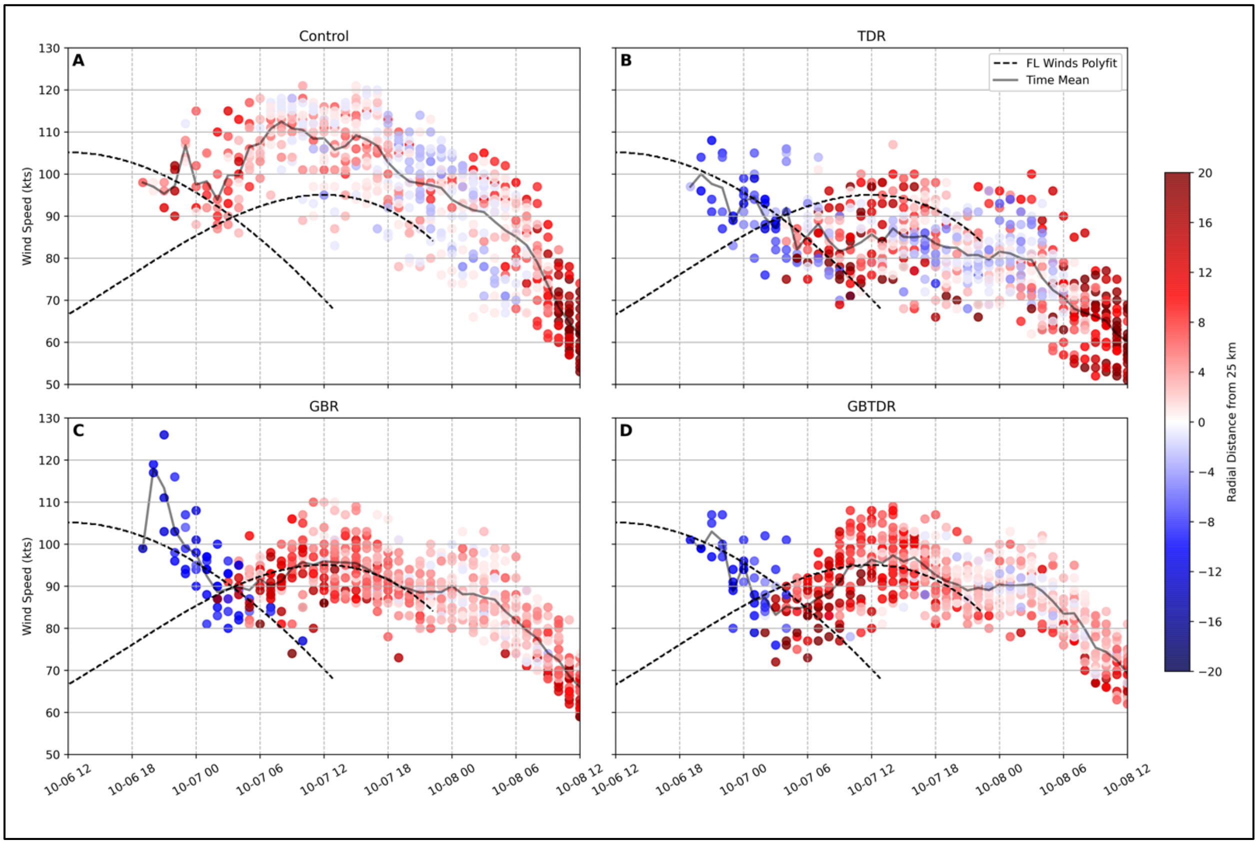

Figure 3.11: Vmax intensity forecasts initialized after 1800 UTC October 6 with color corresponding to the Vmax distance from 25 km radius from the storm center, as in Figure 3.10B. The grey curve represents the time average of all analyses/forecasts valid at each date. The CFs for FL wind maxima are overlayed on each panel to show approximate trends of the two eyewalls. They do not serve as a proxy for the 10m wind intensity.

UTC to 1800 UTC October 6 time period largely show incorrect structural and intensity changes due to poorly initialized structure in all experiments. The grey line in Figure 3.11 corresponds to the time average of the Vmax forecasts, as in Figure 3.9. The CFs for both eyewalls from FL observations are plotted as dashed black curves to show the intensity trends of the two eyewalls and when the change in phase from weakening to reintensification occurs. As mentioned for Figure 3.10B, these CFs are not meant to serve as a proxy for storm intensity due to the difference in vertical levels, but to show trends. Focusing on the GBR and GBTDR experiments, the switch from downward to upward intensity trend correspond nicely with the clear transition from blue to red intensity points. Physically, this represents that as the forecasts switch from weakening to intensifying, the location of the maximum wind switches from the primary (blue colored Vmax point) to secondary (red color Vmax point), meaning the correct structural changes of the decay (strengthening/contraction) or the primary (secondary eyewall) in many of the forecasts are occurring. Similar to Figure 3.10, the intensity changes can be understood conceptually as the forecasts capturing the maximum value of the CFs given the Vmax will be located in whichever eyewall is strongest at the time. During the reintensification of the GBR and GBTDR forecasts, the color of the Vmax points switches from darker to lighter red, indicating that the secondary eyewall is contracting inward. In contrast to GBR and GBTDR, the TDR does not show as clear of a switch in the radius of the Vmax forecasts. Some contrast in the colors of the Vmax points exist around 0200 UTC October 7, which correspond to the four aforementioned forecasts from this experiment that show correct structural and intensity changes. However, after 0200 UTC October 7, the Vmax points colors tend to be mixed between blue and red, as many of the forecasts are not capturing the ERC. Lastly, the Vmax values for Control show a general contraction during the forecasts (red Vmax points becoming lighter red or blue) up until about 0800 UTC October 7, which corresponds to the end of the contraction in the time average structural forecasts in Figure 3.6A. After this time, the colors of the Vmax points are mixed between red and blue, approximately averaging to 0. This agrees with Figure 3.7A, where the time average radius of the primary eyewall in the forecasts stays about constant until 0300 UTC October 8, after which it begins to expand.

To emphasize the importance of correctly initialized structure of the wind field in the experiments, mechanisms for the decay (strengthening/contraction) of the primary (secondary) eyewall during the ERC are discussed using a comparison of free forecasts between the Control and GBR experiments at the 1900 UTC October 6 analysis time as an example. The purpose is not to provide any new insight on possible mechanisms related to ERC dynamics, but to discuss the roles of unbalanced and balanced dynamics in an axisymmetric framework to show general consistency of the ERC evolution in experiments with the existing literature. Furthermore, it has been shown in this study that the accuracy of the forecasts is related to the analyzed structure of CEs, making an examination of the mechanisms for ERC during the weakening and reintensification phases necessary to solidify the importance of correctly analyzed storm structure.

Figure 3.12 shows the evolution of the following azimuthally averaged fields for the Control and GBR free forecasts initialized at 1900 UTC October 6: tangential wind (purple contours), transverse circulation (quivered), absolute angular momentum (black contours) and absolute angular momentum advection (contour filled). Dashed contours are shown for the tangential wind and angular momentum fields so that their evolution can be easily tracked. Figure 3.12B shows

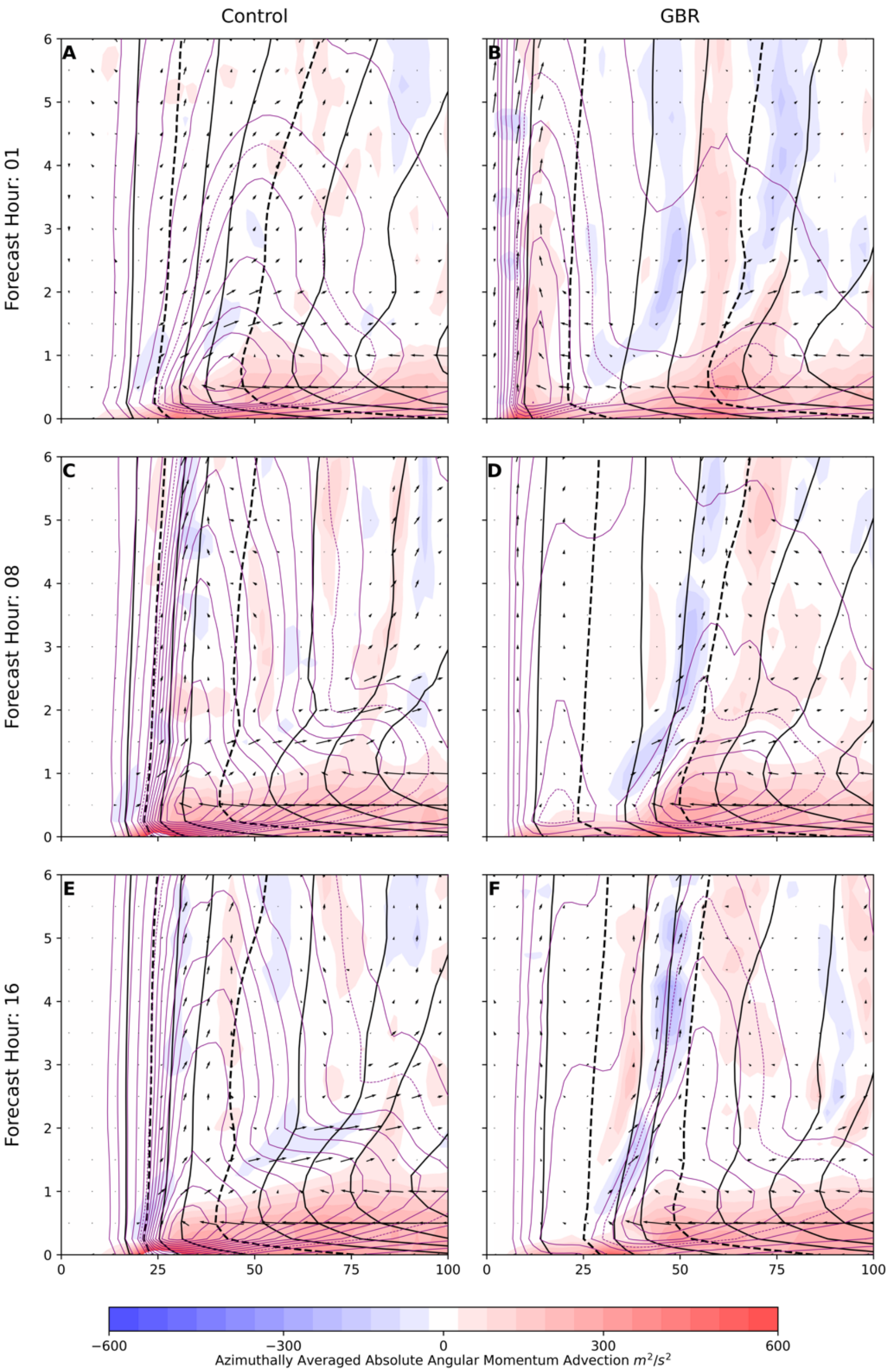

Figure 3.12: Evolution of azimuthally averaged: tangential winds (purple contours), absolute angular momentum (black contours), transverse circulation (quivered), and advection of absolute angular momentum (filled) for Control and GBR experiment initialized at 1900 UTC October 6. Two contours in both the azimuthally averaged tangential winds and absolute angular momentum are dashed so that their changes can be tracked.

the one-hour forecast for the GBR experiment where several features are noticeable. First, there are two wind maxima present in the azimuthal average, with the primary wind maximum being more vertically deep and stacked, whereas the secondary wind maximum is shallower and slopes outward in radius with height. In addition, each wind maxima have their own transverse circulation associated with it, characterized by the radial inflow in the lower levels, turning vertically upward at the eyewall, and finally flowing radially outward at some height (in/up/out).

The dynamics governing the axisymmetric intensification and contraction of the secondary eyewall can be explained using both balanced (Shapiro & Willoughby , 1982; Willoughby et al., 1982) and unbalanced (Huang et al., 2012; Smith et al., 2009) mechanisms. The balanced mechanism describes the evolution of convection in a rotating fluid, which drives a transverse circulation through the heating source. This results in radial convergence of absolute angular momentum surfaces (M) above the boundary layer (where it is approximately conserved), resulting in a radial expansion of the tangential wind field and its contraction as the maximum in its tendency lies radially inward of the heat source. Overall, this increases the intensity of the secondary eyewall while also contracting it radially inward. Unbalanced dynamics associated with the intensification of the secondary eyewall takes place in the boundary layer (BL) where M is not materially conserved due to frictional dissipation. If the radial inflow is strong enough to move larger M surfaces radially inward with minimal loss of M due to friction, tangential winds in the BL can become supergradient, leading to a rapid deceleration of the radial flow at the eyewall, and the enhancement of the transverse circulation as the BL inflow tuns up and out of the eyewall (Smith et al., 2009). This unbalanced mechanism can then lead to further intensification via the balanced mechanism. For the sake of simplicity in the analysis that follows, 500 m AGL and below will be considered the BL.

The balanced mechanism can be seen in Figure 3.12 B,D, F, where radial inflow around 1km results in positive M advection above the BL. Unbalanced dynamics are manifested in the strong radial advection of M in the BL where the largest positive M advection lies. This results in supergradient winds (not shown) in the BL that help to enhance the transverse circulation associated with the secondary eyewall, and further intensify it via the balanced mechanism. The overall effects of these two mechanisms in the axisymmetric framework are to 1: contract the secondary eyewall inward, as the maximum in positive M advection lies just radially inward of the tangential wind maximum, 2: intensify the secondary wind maximum as evidenced by the evolution of the dashed contour for the tangential wind field, and 3: expand the wind field associated with the secondary eyewall radially outward and vertically.

The dynamical mechanisms associated with the decay of the primary are less solidified in literature than those of the secondary eyewall's contraction and strengthening, including both kinematic and thermodynamic explanations associated with the interaction of the two eyewalls. Mechanisms such as the cutoff of high moist entropy air to the inner eyewall (Bell et al., 2012; Zhou & Wang, 2011b) and suppression of the primary eyewall convection due to subsidence induced by the secondary eyewall (Rozoff et al., 2008; Shapiro & Willoughby, 1982; Willoughby et al., 1982) were not found to be consistent or prominent features in the experiments. Instead, the decay of the primary eyewall can be at least partially explained in a simple kinematic sense put forth by Rozoff et al. (2008). The mechanism involves the cutoff of high M air to the primary eyewall due to the enhanced transverse circulation associated with the growing and intensifying secondary eyewall. Figure 3.12B shows a robust transverse circulation and tangential wind maximum associated with the primary eyewall, where positive M advection exists at the primary eyewall. The reason for this positive advection of M at the primary eyewall is the radial inflow being able to penetrate the secondary eyewall to reach the primary eyewall. As the forecast evolves and the secondary eyewall beings to intensify, the associated transverse circulation grows stronger. The inflow above the inflow layer is cut off from reaching the primary eyewall, resulting in the spindown of the primary tangential wind maximum as evidenced by the radially outward movement of the dashed M contour. By forecast hour 16 (Figure 3.12F), the primary wind maximum in the azimuthal average has almost disappeared, as the radial inflow and positive advection of M is cutoff by the secondary eyewall.

In complete contrast to the structure shown in the GBR forecast for this analysis time, the Control only shows the evolution of a single eyewall that can be explained with balanced and unbalanced dynamics that results in a contracting and strengthening primary wind maximum. These diagnostics show that if a concentric eyewall structure exists in the analysis, simple balanced and unbalanced dynamics can partially explain the evolution of the ERC in an axisymmetric framework. Because these changes are tied specifically to the impacts the secondary eyewall has on the existing primary eyewall, without proper initialization of concentric eyewalls, the mechanisms for the ERC cannot take place.

4. Discussion and Conclusions

In this study, hourly DA cycling was performed for Hurricane Matthew during a 24-hour time period from 1500 UTC October 6 to 1500 October 7, 2016, assimilating GBR and TDR observations together, as well as separately using HWRF and the Hybrid 3DEnVar DA system for the analysis and prediction of Matthew's ERC. The results of this study show that the temporal availability, including duration, of ICDR observations are important for capturing the correct evolution of Matthew's ERC. Comparison of the GBR experiment, which has continuous access to GBR observations from 1500 UTC October 6 to 1500 UTC October 7, and the TDR experiment which has continuous access to TDR observations from 1900 UTC October 6 to 0100 UTC October 7, show stark differences in the establishment of CE structure and evolution of the primary and secondary eyewalls throughout the ERC (Figure 3.4). The GBR experiment corrects the initially inaccurate background storm structure earlier, resulting in a CE structure that evolves consistent with FL RECON observations throughout the rest of the cycling, showing the eventual decay of the primary eyewall and the contraction/strengthening of the secondary eyewall throughout the weakening and reintensification phases. The TDR experiment, with later and fewer hours of availability, shows less consistent CE structure, and the inability to capture the strengthening and contraction of the secondary eyewall after observations become unavailable. The biggest takeaway from the analyses' structural evolutions is that without early availability and long duration of ICDR observations, Matthew's structural changes cannot be analyzed consistently throughout the ERC. In addition, the lack of ICDR observations altogether in the Control experiment shows the complete inability to initialize CE structure during the cycling. These effects were shown to carry over to the quality of the forecasts.

Differences in 3D ICDR observation distributions were also shown to affect the initialization of intricate features associated with Matthew's ERC. The GBR experiment, despite very limited lower-level observation coverage, was able to initialize CEs through DA cycling that included both corrections to the upper-level wind field, and extension of those winds to the surface during the time integration. A comparison with FL RECON observations shows that although CEs were established during the DA cycling, the GBR experiment has a tendency to contract the primary and secondary eyewalls too far radially inward, in part due to the lack of observation coverage at lower levels. The TDR, in comparison, demonstrates the ability to correct the initially inconsistent storm structure to a CE TC in only one cycle due to superior horizontal and vertical observation coverage. However, the TDR horizontal observation distribution can vary drastically from cycle to cycle depending on whether the flight is in a penetration or downwind leg during the DA time window. Limited or incomplete horizontal coverage during downwind legs is hypothesized to contribute to the less consistent TDR analyses during their availability, consistent with the findings of Aksoy et al. (2012). These results highlight the importance of accounting for the horizontal variability of ICDR observations during the DA time window. A proposed method to account for the horizontal variability during high-frequency cycling is to use the hourly FGAT method. This would require further investigation to determine its ability to more effectively use the TDR observations from downwind legs.

The simultaneous assimilation of TDR and GBR observations shows the ability to complement each other when their vertical distributions differ. At 1900 UTC October 6, the deficiencies in the GBR experiment relating to the spuriously small primary eyewall and inwardly displaced secondary eyewall are corrected when the two observation sets are assimilated together. The differences in the structural evolution between the GBR and GBTDR experiments shown throughout the entire cycling period in Figure 3.4 are small, with the most noticeable being the earlier intensification of the secondary eyewall in the GBR experiment. These small differences in the azimuthally averaged tangential wind evolution are not completely representative of the differences between the 3D structure of the experiments. However, they do suggest that the dominant structural features in the analyses result from the initial establishment of CE structure due to the early availability of the GBR observations, with TDR observations making small contributions to correcting the storm structure thereafter.

A notable point relating to the simultaneous assimilation of both GBR and TDR observations which was not discussed in Section 3 is the establishment of vertical vortex tilt at select analysis times due to the differences in spatial and temporal observation distributions, specifically during penetration legs of the TDR flight. This is best described with a brief example at 1900 UTC for the GBTDR experiment. Because the flight passed through the center of Matthew at 1917 UTC (center fix time), or 17 minutes past the analysis time, the observations suggest the storm center is located farther to the northwest, in the direction of the storm motion, compared to its observed location at 1900 UTC. The GBR observations on the other hand, are distributed more uniformly in time, and suggests the storm center is closer to the observed location at the analysis time. Due to the assumption in the 3DEnVar method that all observations within the hour-long time window are valid at the analysis time, the result of the DA is to shift the storm center at the lower levels (where TDR coverage is superior) towards the location at which the plane found Matthew's center, and shift the storm center at the middle to upper levels (where GBR coverage is superior) towards the observed location at the analysis time. This problem becomes more accentuated when the center fix time of the plane is further away from the analysis time. It is not seen, however, in either the GBR or GBTDR experiments when these two ICDR observation types are assimilated by themselves. Preliminary tests (not shown) show the hourly FGAT method to be a potential remedy to this problem by accounting for the temporal distribution of the observations. However, this method did not remove all of the vortex tilt, which could result from many possibilities, one of which includes the hourly FGAT method's assumption that the state variables change linearly throughout the DA time window. This subject will require more research to determine what the best solution may be; however, it is pivotal for the future assimilation of these ICDR observation types simultaneously. It should also be noted that the vortex tilt in the select analysis times of the GBTDR experiment was determined not to be detrimental to the resulting free forecasts, as the vortex tilt vanishes early in the time integration due to the environmental wind shear not being supportive of large tilt during the time period of TDR availability.

The deterministic forecasts launched from experiments with initialized CEs were shown to capture both the correct structural and intensity changes associated with the weakening and reintensification phases of the ERC which can be explained by unbalanced and balanced dynamics associated with interactions of the two eyewalls. The GBR and GBTDR experiments show the consistent ability to capture the downward and upward intensity trends associated with these two phases that are clearly exhibited in the time mean of Vmax forecasts throughout the cycling. In addition, the timing of the phase switch and the ending of the ERC correspond well with FL RECON observations, indicating that these experiments are able to make accurate and consistent forecasts of the subtle intensity changes that are systematically documented for these two phases of the ERC. The consistency between the structural changes seen in the Hovmöller diagrams and point intensity forecasts verify that the intensity trends are directly tied to the structural changes during the ERC. This is an encouraging result for the future of TC intensity prediction, given the reliance on point intensity forecasts such as Vmax for operational use. The TDR experiment does not consistently show these intensity changes due to the aforementioned poor analysis structure in many of its initializations throughout the cycling. The GBR and GBTDR experiments' superior structure in their analyses throughout the entirety of the ERC was shown to be responsible for the more accurate intensity forecasts.

Given the fixed nature of GBR radar sites, every TC case has the potential to be unique in terms of availability and spatial distribution of both GBR and TDR observations. In this study, the GBR observations were the first to provide inner core coverage of Matthew, with the TDR availability lagging behind, which may not be the case for every storm. Additionally, the over 24 hours of GBR availability provided a unique way to study an ERC case due to Matthew's paralleling of Florida's coast with minimal interaction with land. In general, a systematic study is needed to assess model performance when assimilating both types of ICDR observations to account for a variety of possibilities of temporal availability and spatial coverage. Additionally, more cases involving ERC prediction need to be performed to assess if the analysis and prediction of these events can demonstrate accuracy for other TCs that may be initialized at different points in the ERC and have different CE structure.

Bibliography

Abarca, S. F., & Corbosiero, K. L. (2011). Secondary eyewall formation in WRF simulations of Hurricanes Rita and Katrina (2005). *Geophysical Research Letters, 38*, 1-5.

Aksoy, A., Aberson, S. D., Vukicevic, T., Sellwood, K. J., Lorsolo, S., & Zhang, X. (2013). Assimilation of high-resolution tropical cyclone observations with an Ensemble Kalman Filter using NOAA/AOML/HRD's HEDAS: Evaluation of the 2008-11 vortex-scale analyses. *Monthy Weather Review, 141*, 1842-1865.

Aksoy, A., Lorsolo, S., Vukicevic, T., Sellwood, K. J., Aberson, S. D., & Zhang, F. (2012). The HWRF hurricane ensemble data assimilation system (HEDAS) for high-resolution data: The impact of airborne doppler radar observations in an osse. *Monthly Weather Review, 140*, 1843-1862.

Bell, M. M., Montgomery, M. T., & Lee, W.-C. (2012). An axisymmetric view of concentric eyewall evolution in Hurricane Rita (2005). *Journal of the Atmospheric Sciences, 69*, 2414-2432.

Biswas, M. K., Abarca, S., Bernardet, L., Ginis, I., Grell, E., Iacono, M., . . . Winte. (2018, November). *Hurricane Weather Research and Forecasting (HWRF) Model: 2018 Scientific Documentation.* Retrieved from Developmental Testbed Center: https://dtcenter.org/sites/default/files/community-code/hwrf/docs/scientific_documents/HWRFv4.0a_ScientificDoc.pdf

Cangialosi, J. P., Blake, E., DeMaria, M., Penny, A., Latto, A., Rappaport, E., & Tallapragada, V. (2020). Recent progress in tropical cyclone intensity forecasting at the National Hurricane Center. *Weather and Forecasting, 35*(5), 1913-1922.

Corbosiero, K. L., & Molinari, J. (2003). The relationship between storm motion, vertical wind shear, and convective asymmetries in tropical cyclones. *Journal of Atmospheric Science, 60*, 366-376.

Creating a New Suite of Statistical Models that Predict the Onset of an Eyewall Replacement Cycle. (n.d.). Retrieved July 2021, from National Centers for Environmental Prediction: https://www.ncdc.noaa.gov/news/creating-new-suite-statistical-models-predict-onset-eyewall-replacement-cycle

Didlake, A. C., Heymsfield, G. M., Reasor, P. D., & Gumond, S. R. (2017). Concentric eyewall asymmetries in Hurricane Gonzalo (2014) observed by airborne radar. *Monthy Weather Review, 145*, 729-749.

Dong, J., & Xue, M. (2013). Assimilation of radial velocity and reflectivity data from coastal WSR-88D radars using an ensemble Kalman filter for the analysis and forecast of landfalling hurricane Ike (2008). *Quarterly Journal of the Royal Meteorological Society, 139*, 467 – 487.

Ferrier, B. (2005). An efficient mixed-phase cloud and precipitation scheme for use in Operational NWP Models. *AGU Spring Meeting.*

Fischer, M. S., Rogers, R. F., & Reasor, P. D. (2020). The rapid intensification and eyewall replacement cycles of Hurricane Irma (2007). *Monthly Weather Review, 148*, 981-1004.

Fisher, M., & Anderson, E. (2001). *Developments in 4D-Var and Kalman Filtering.* European Centre for Medium Range Weather Forecasts.

Gall, R., Franklin, J., Marks, F., Rappaport, E. N., & Toepfer, F. (2013). The hurricane forecast improvement project. *Bulletin of the American Meteorological Society, 94*, 329–343.

Helmus, J. J., & Collis, S. M. (2016). The Python ARM Radar Toolkit (Py-ART), a library for working with weather radar data in the Python programming language. *Journal of open research software, 4*(1).

Houze, R. A., Chen, S. S., Smull, B. F., Lee, W.-C., & Bell, M. M. (2007). Hurricane intensity and eyewall replacement. *Science, 315*, 1235-1239.

Huang, Y.-H., Montgomery, M. T., & Wu, C.-C. (2012). Concentric eyewall formation in Typhoon Sinlaku (2008). Part II: Axisymmetric dynamical processes. *Journal of the Atmospheric Sciences, 69*(2), 662-674.

Irish, J. L., Resio, D. T., & Ratcliff, J. J. (2008). The influence of storm size on hurricane surge. *Journal of Physical Oceanography, 38*(9), 2003-2013.

Kepert, J. D. (2013). How does the boundary layer contribute to eyewall replacement cycles in aximsymmetric tropical cyclones? *Journal of the Atmospheric Sciences, 70*, 2808-2829.

Kossin, J. P., & Sitkowski, M. (2009). An objective model for identifying secondary eyewall formation in hurricanes. *Monthly Weather Review, 137*(3), 876–892.

Kossin, J. P., & Sitkowski, M. (2012). Predicting hurricane intensity and structure changes associated with eyewall replacement cycles. *Weather and Forecasting, 27*(2), 484-488.

Landsea, C. W., & Cangialosi, J. P. (2018). Have we reached the limits of tropical cyclone track forecasting? *Bulletin of the American Meteorological Society, 99*(11), 2237–2243.

Landsea, C. W., & Franklin, J. L. (2011). Atlantic hurricane database uncertainty and presentation of a new database format. *Monthly Weather Review, 141*(10), 3576-3592.

Li, Y., Wang, X., & Xue, M. (2012). Assimilation of radar radial velocity data with the WRF hybrid ensemble-3DVAR system for the prediction of Hurricane Ike (2008). *Monthly Weather Review, 140*, 3507-3524.

Lu, X., Wang, X., Li, Y., Tong, M., & Ma, X. (2017). GSI-based ensemble-variational hybrid data assimilation for HWRF for hurricane initialization and prediction: impact of various error covariances for airborne radar observation assimilation. *Quarterly Journal of the Royal Meteorological Society, 143*, 223-239.

Lu, X., Wang, X., Tong, M., & Tallapragada, V. (2017). GSI-based, continuously cycled, dual-resolution hybrid ensemble-variational data assimilation system for HWRF: System description and experiments with Edouard (2014). *Monthly Weather Review, 145*(12), 4877-4898.

Maclay, K. S., DeMaria, M., & Vonder Haar, T. H. (2008). Tropical cyclone inner-core kinetic energy evolution. *Monthly Weather Review, 136*(12), 4882-4898.

Rozoff, C. M., Schubert, W. H., & Kossin, J. P. (2008). Some dynamical aspects of tropical cyclone concentric eyewalls. *Quarterly Journal of the Royal Meteorological Society, 134*, 583-593.

Shapiro, L. J., & Willoughby , H. E. (1982). The response of balanced hurricanes to local sources of heat and momentum. *Journal of the Atmospheric Sciences, 39*, 378-394.

Sippel, J. (2019). Tropical Cyclone Modeling and Data Assimilation. *WMO Workshop at NHC.*

Sitkowski, M., Kossin, J. P., & Rozoff, C. M. (2011). Intenisty and strucutre changes during hurricane eyewall replacement cycles. *Monthly Weather Review, 139*, 3829-3847.

Smith, R. K., Montgomery, M. T., & Van Sang, N. (2009). Tropical cyclone spin-up revisited. *Quarterly Journal of the Royal Meteorological Society, 135*, 1321-1335.

Stewart, S. R. (2017). *National Hurricane Center tropical cyclone report: Hurricane Matthew.* National Hurricane Center.

Terwey, W. D., & Montgomery, M. T. (2008). Secondary eyewall formation in two idealized, full physics modeled hurricanes. *Journal of Geophysical Research, 113*, 1-18.

Torn, R. D. (2010). Performance of a mesoscale ensemble Kalman filter (EnKF) during the NOAA High-Resolution hurricane test. *Monthly Weather Review, 138*(12), 4375-4392.

Wang, M., Xue, M., & Zhao, K. (2015). The impact of T-TREC-retrieved wind and radial velocity data assimilation using EnKF and effects of assimilation window on the analysis and prediction of Typhoon Jangmi (2008). *Journal of Geophysical Research: Atmospheres, 121*, 259–277.

Wang, M., Xue, M., Zhao, K., & Dong, J. (2014). Assimilation of T-TREC-Retrieved winds from Single-Doppler radar with an ensemble kalman filter for the forecast of Typhoon Jangmi (2008). *Monthly Weather Review, 142*, 1892-1907.

Wang, Y. (2008). Rapid filamentation zone in a numerically simulated tropical cyclone. *Journal of the Atmospheric Sciences, 65*(4), 1158-1181.

Wang, Y. (2008). Stucture and formation of an annular hurricane simulated in a fully compressible, nonhydrostatic model-TCM4. *Journal of the Atmospheric Sciences, 65*(5), 1505-1527.

Weng, Y., & Zhang, F. (2012). Assimilating airborne doppler radar observations with an ensemble kalman filter for convection-permitting hurricane initialization and prediction: Katrina (2005). *Monthly Weather Review, 140*, 841-859.

Willoughby, H. E., Clos, J. A., & Shoreibah, M. G. (1982). Concentric eye walls, secondary wind maxima, and the evolution of the hurricane vortex. *Journal of the Atmospheric Sciences, 39*, 395-411.

Zhang, F., Weng, Y., Gamache, J. F., & Marks, F. D. (2011). Performance of con vection-permitting hurricane initialization and prediction during 2008-2010 with ensemble data assimilation of inner-core airborne Doppler radar observations. *Geophysical Research Letters, 38*.

Zhang, F., Weng, Y., Sippel, J. A., Meng, Z., & Bishop, C. H. (2009). Cloud-resolving hurricane initialization and prediction through assimilation of doppler radar observations with an ensemble kalman filter. *Monthy Weather Review, 137*(7), 2105-2125.

Zhang, Q.-H., Kuo, Y.-H., & Chen, S.-J. (2005). Interaction between concentric eye-walls in super typhoon Winnie (1997). *Quartery Journal of the Royal Meteorological Society, 131*, 3183-3204.

Zhao, K., & Xue, M. (2009). Assimilation of coastal Doppler radar data with the ARPS 3DVAR and cloud analysis for the prediction of Hurricane Ike (2008). *Geophysical Research Letters, 36*.

Zhou, X., & Wang, B. (2009). From concentric eyewall to annular hurricane: A numerical study with the cloud-resolved WRF model. *Geophysical Research Letters, 36*, 1-5.

Zhou, X., & Wang, B. (2011). Mechanism of concentric eyewall replacement cycles and associated intensity change. *Journal of the Atmospheric Sciences, 68*, 972-988.

Zhu, L., Wan, Q., Shen, X., Meng, Z., Zhang, F., Weng, Y., . . . Yue, J. (2016). Prediction and predictability of high-impact western pacific landfalling tropical cyclone Vicente (2012) through convection-permitting ensemble assimilation of doppler radar velocity. *Monthly Weather Review, 144*, 21-43.